Supporting Information

Electrocatalytic Nitrate Reduction on Oxide-Derived Silver with Tunable Selectivity to Nitrite and Ammonia

Hengzhou Liu,[a] Jaeryul Park,[a] Yifu Chen,[a] Yang Qiu,[b] Yan Cheng,[a] Kartik Srivastava,[a] Shuang Gu,[c] Brent H. Shanks,[a] Luke T. Roling,[*a] Wenzhen Li[*a, d]

[a] Department of Chemical and Biological Engineering, Iowa State University, 618 Bissell Road, Ames, IA 50011 (USA).

[b] Institute for Integrated Catalysis, Energy and Environment Directorate, Pacific Northwest National Laboratory, 902 Battelle Blvd., Richland, WA 99352 (USA).

[c] Department of Mechanical Engineering, Wichita State University, 1845 Fairmount St, Wichita, KS 67260 (USA).

[d] US Department of Energy Ames Laboratory, 2408 Pammel Drive, Ames, IA 50011 (USA).

*To whom correspondence should be addressed:

Wenzhen Li: wzli@iastate.edu, Luke T. Roling: roling@iastate.edu

Table of Contents

Experimental Section

1. Chemicals

All chemicals were used as received without purification. Silver foil (0.5 mm thick, 99.9985%), copper foil (0.5 mm thick, 99.9985%), platinum foil (0.025 mm thick, 99%), tin foil (0.025 mm thick, 99.9%), titanium foil (0.89 mm thick, 99.7%), zinc foil (0.1 mm thick, 99.994%), iron foil (0.5 mm thick, 99.99%), nickel foil (0.1 mm thick, 99.5%), palladium foil (0.025 mm thick, 99.9%), gold foil (0.05 mm thick, 99.95%), lead foil (0.76 mm thick, 99.8%), molybdenum foil (0.1 mm thick, 99.95%), tungsten foil (0.25 mm thick, 99.95%), aluminum foil (0.1 mm thick, 99.99%), cobalt foil (0.1 mm thick, 99.95%), zirconium foil (0.2 mm thick, 99.8%), vanadium foil (1.0 mm thick, 99.5%), and hydroxylamine hydrochloride ($NH_2OH{\cdot}HCl$, 99%) were purchased from Alfa Aesar. Bismuth plate (>99.99%) was purchased from Amazon. Potassium nitrate (KNO_3, 99.7%), potassium chloride (KCl, 100%), potassium phosphate dibasic (K_2HPO_4, ≥98%), potassium phosphate monobasic (KH_2PO_4, ≥99%), sodium carbonate (Na_2CO_3, 100%), sodium chloride (NaCl, ≥99%), sodium sulfate (Na_2SO_4, ≥99%), sodium bicarbonate ($NaHCO_3$, 100%), hydrogen peroxide (H_2O_2, 30%), nitric acid (HNO_3, 70%), hydrochloric acid (HCl, 37%), phosphoric acid (H_3PO_4, ≥85%), and methanol (HPLC grade) were purchased from Fisher Chemical. Sodium salicylate (≥99.5%), sodium hydroxide (NaOH, ≥97%), potassium hydroxide (KOH, ≥85%), sodium nitroferricyanide dihydrate ($Na_2[Fe(CN)_5NO]{\cdot}2H_2O$, ≥99%), sodium hypochlorite solution (NaOCl, available chlorine 4.00–4.99%), *N*-(1-Naphthyl)ethylenediamine dihydrochloride (NED, ≥97%), sulfanilamide (≥99%), and palladium on active carbon (Pd/C, 5 wt.% Pd loading) were purchased from Sigma-Aldrich. Silver nanopowder (80–100 nm, 99.99%) was purchased from US Research Nanomaterials, Inc. Potassium nitrite (KNO_2, 97%), lead(II) nitrate ($Pb(NO_3)_2$, ≥99%), and *n*-Octylamine (>99%) were purchased from Acros Organic. 8-quinolinol was purchased from TCI. Ammonia standard solution (100 mg L^{-1} as NH_3-N) was purchased from Hach. Silver standard solution (1,000 μg mL^{-1} of Ag^+ in 5% v/v nitric acid) was purchased from Inorganic Ventures. Plain carbon cloth, Vulcan XC-72R, PTFE gaskets, and Nafion 115 membrane were purchased from Fuel Cell Store. 40% Pt on Vulcan XC-72 (Pt/C) and IrO_2 powder were purchased from Premetek. Argon (Ar, Ultra High Purity, 99.999%), hydrogen (H_2, Ultra High Purity, 99.999%), and carbon dioxide (CO_2, industrial grade) were purchased from Airgas. H_2 calibration gases (10 ppm, 100 ppm, 1,000 ppm, 5,000 ppm, 10,000 ppm, balance helium) and N_2O calibration gases (95 ppm, 1,000 ppm, balance nitrogen) were purchased from Cal Gas Direct. Nitrogen (N_2) calibration gases (100 ppm, 1,000 ppm, 10,000 ppm, 100,000 ppm, balance helium) were purchased from Shop Cross. Nitrogen oxides detector tube (No. 175U, 1–60 ppm) was purchased from Kitagawa America. Deionized (DI) water (18.2 MΩ cm, Barnstead™ E-Pure™) was used for all experiments in this work.

2. Preparation of working electrodes

Oxide-derived silver (OD-Ag) was prepared in a standard three-electrode system by a modified square wave voltammetric (SWV) method according to Ma *et al.*[16] A polycrystalline silver foil (0.5 mm thick, 99.9985%, Alfa Aesar), a silver/silver chloride (Ag/AgCl) electrode (saturated KCl, E^0 = 0.197 V *vs.* SHE, Pine Research), and a platinum foil were used as the working electrode, reference electrode, and counter electrode, respectively. 0.2 M NaOH was used as the electrolyte. To synthesize OD-AgO_x, symmetric square-wave pulse potential from 0 to 1 $V_{Ag/AgCl}$

was applied by a Biologic SP-300 potentiostat/galvanostat on the Ag foil at a frequency of 500 Hz for 3 h (Supplementary movie 1, with a 16X play rare). Then, a constant potential (−1.30 $V_{Ag/AgCl}$) was applied for 10 min to reduce OD-AgO_x to OD-Ag.

The electrode with Ag nanoparticles (80–100 nm, 99.99%, US Research Nanomaterials) on Ag foil (Ag NPs/Ag) was prepared by airbrushing a 2-propanol dispersion of Ag NPs (10 mg mL^{-1}) and Nafion on both sides of the Ag foil. The mass ratio of Ag NPs and Nafion was 4:1. The catalyst loading was controlled at 1.5 $mg_{Ag}\,cm^{-2}$.

3. Electrocatalytic and catalytic activity measurements

3.1 Electrochemical measurements Electrochemical measurements.

Linear sweep voltammetry (LSV) measurements were carried out in a single-compartment cell with a three-electrode configuration without stirring. The electrolyte consisted of 0.1 M KCl, and its pH was adjusted to 4 by adding hydrochloric acid. The scan rate was 5 mV s^{-1}.

The electrochemical reduction of NO_3^- (NO3RR) was performed by chronoamperometry (CA) at room temperature in a dual-chamber H-type cell with a three-electrode configuration, and the cathode chamber was airtight. Each chamber contained 15 mL of the electrolyte (0.1 M KCl, pH = 4) and the two chambers were separated by a Nafion 115 membrane (K^+ form). KNO_3 was added to the catholyte, which was magnetically stirred at 350 r.p.m. by a PTFE-coated stir bar (20 × 6 mm). The geometric area of the working electrode was chosen depending on the experimental conditions, typically 2, 4, or 6 cm^2. Specifically, at low overpotentials and NO_3^- concentration such as −1.00 and −1.10 $V_{Ag/AgCl}$ with 0.01 M NO_3^-, a 6 cm^2-electrode was used to ensure the reaction was complete in a few hours. At high overpotentials or NO_3^- concentration, smaller electrodes were used to avoid overload of the potentiostat. A graphite rod was used as the counter electrode. All electrode potentials were measured against the Ag/AgCl reference electrode (saturated KCl) with 85% *iR*-compensation. Ar was fed into the catholyte at a flow rate of 12.5 mL min^{-1}. The outlet gas from the cathode chamber was bubbled into an external trapping solution containing 25 mL of 0.1 M KCl (pH = 3) to absorb any NH_3 that evolved from the system. The gas flow was then introduced to the on-line gas chromatography (GC) to quantify H_2. The duration of CA was chosen depending on the total applied charge, as detailed in the Figures captions. The current density was calculated based on the geometric area (for both sides) of the electrode. The entire experimental setup is shown in **Figure S8**.

The conversion of NO_3^- (X) and selectivity to product i (S_i, i = NH_4^+, NO_2^-, or NH_2OH) were calculated by

$$X = \frac{n_0 - n}{n_0} \times 100\%$$

$$S_i = \frac{n_i}{n_0 - n} \times 100\%$$

where n_0 is the initial amount of NO_3^- (mol); n is the amount of NO_3^- after electrolysis (mol); n_i is the amount of product i (mol).

The faradaic efficiency of product i (FE_i) was calculated by

$$FE_i = \frac{n_i z_i F}{Q} \times 100\%$$

where z_i is the number of electrons transferred to product i; F is the Faraday constant (96,485 C mol^{-1}); Q is the total charge (C) passed through the electrolytic cell.

3.2 Catalytic reduction of NO_2^-

Catalytic reduction of NO_2^- was carried out at room temperature in a gastight reactor. Specifically, 50 mg of Pd/C was suspended in 15 mL of the NO_2^--containing solution which was magnetically stirred at 800 r.p.m. The solution was sparged with CO_2 at 25 mL min^{-1} by a gas dispersion tube (Ace Glass, 7 mm O.D., 25–50 micron porosity) during the test to maintain the CO_2-buffered condition.[1] After the solution was saturated with CO_2 (pH ~7), H_2 was fed at 25 mL min^{-1} via another gas dispersion tube. During the measurement, the solution was sampled periodically from the reactor, followed by dilution and filtration for product analysis.

The observed reaction rate constant k_{obs} (min^{-1}) was calculated assuming pseudo-first-order dependence on NO_2^- concentration (H_2 is in excess) by

$$\frac{dc}{dt} = -k_{obs} c$$

where c is the concentration of NO_2^- (mg L^{-1}) and t is the reaction time (min). The rate constant was normalized to the concentration of surface Pd in the solution by[2]

$$k = \frac{k_{obs}}{\frac{AmM}{aN_A V}}$$

where A is the active surface area of Pd (m^2 g^{-1}), m is the mass of Pd in the reactor (0.050 g), M is the molar mass of Pd (106.42 g_{Pd} mol^{-1}), a is the cross-sectional area of one Pd atom (7.87 × 10^{-20} m^2), N_A is the Avogadro constant (6.02 × 10^{23} mol^{-1}), V is the volume of the NO_2^--containing solution (0.015 L). The unit of the normalized k calculated from the above equation is L g_{Pd}^{-1} min^{-1}.

3.3 Combined process for agricultural wastewater denitrification

The combined denitrification process was carried out in three media: 1) 0.1 M KCl; 2) simulated waste stream from ion-exchange columns (containing 400 mg L^{-1} of NaCl, 400 mg L^{-1} of Na_2SO_4, and 8,000 mg L^{-1} of $NaHCO_3$ in DI water);[3] and 3) real agricultural wastewater obtained from Des Moines Water Works, Iowa (filtered to remove the insoluble matters). Additional KNO_3 was added to set the concentration of NO_3^- at 0.01 M (corresponding to 140

ppm-N) to simulate the NO_3^- content enriched in waste streams. The two-step denitrification treatment was performed as described in electrochemical measurements (for NO_3^- to NO_2^-) and catalytic measurements (for NO_2^- to N_2).

We also utilized a proton-exchange membrane (PEM)-based water electrolyzer to generate on-site H_2 for the second step (catalytic reduction of NO_2^-) (**Figure S29**). The membrane electrode assembly (MEA) consisted of a Pt/C cathode, IrO_2 anode, and a Nafion 115 membrane (H^+ form). The electrodes were prepared by spraying the dispersion containing the catalyst and Nafion ionomer (4:1 in mass) onto plain carbon cloths. The catalyst loading was 1.15 mg cm^{-2} (in Pt) for the cathode and 3.75 mg cm^{-2} (in IrO_2, Premetek) for the anode. The MEA was hot-pressed at 130℃ and 1,000 psi for 3 min before assembled into the cell hardware containing two PTFE gaskets (Fuel Cell Store) and two graphite end plates with serpentine flow channels. The active area of the electrodes was 5 cm^2. The cell was operated at 80 ℃ with DI water supplied in both cathode and anode chambers at a flow rate of 5.5 mL min^{-1} by a peristaltic pump. Repeated CV scans were carried out between 0 and 1.6 V until a stable CV curve was obtained. Constant-current electrolysis was then performed at 1.4 A, and the generated H_2 from the cathode compartment was directly sparged in the NO_2^--containing solution.

4. Computational methods

The Vienna *ab initio* Simulation Package (VASP) was used for density functional theory (DFT) calculations.[4-5] Projector augmented-wave (PAW) potentials were implemented to describe electron-ion interactions,[6-7] and the Perdew-Wang functional was used within the generalized gradient approximation (GGA-PW91) to determine exchange-correlation energies.[8] Electronic energies were calculated to a precision of 10^{-4} eV, using a kinetic energy cutoff of 400 eV. Geometry optimizations were performed until the forces on all atoms were less than 0.02 eV Å^{-1}. Optimized lattice constants were calculated as follows (experimental values in parentheses, all values in Å): Ag 4.16 (4.09), Cu 3.64 (3.61), and Pd 3.96 (3.89).[9]

Ag, Pd, and Cu foil electrodes were represented by fcc(111) facets in calculations. The wave-like structure of OD-Ag was represented by the (211) facet of Ag. This was chosen as a first approximation to a surface exposing a higher fraction of undercoordinated metal atoms in comparison to the foil. The (111) surfaces were constructed with 3 × 3 surface unit cells and four metal layers; (211) surfaces were constructed in 1 × 3 unit cells with 12 metal layers. The bottom two layers of (111) cells and bottom six layers of (211) cells were fixed at the bulk-optimized lattice positions and the remaining layers and adsorbate atoms were allowed to fully relax during optimization. The distance between periodic metal slabs was at least 13 Å to minimize interactions between adjacent slabs. The surface Brillouin zone of all prepared surfaces was sampled with a 6 × 6 × 1 *k*-point mesh.[10]

All gas-phase Gibbs free energies (G_x) were calculated in the following manner:

$$G_x = E_x + ZPE_x - TS_x$$

where E_x is the total energy of the adsorbate, ZPE_x is the calculated zero-point energy correction of x, T is the absolute temperature (298 K), and S_x is the calculated entropy of x. *ZPE* and *S* were estimated from vibrational frequency calculations of adsorbed species, including translational, vibrational, and rotational modes. Estimates were obtained using a second-order finite difference numerical differentiation of forces and a step size of 0.015 Å, assuming a harmonic oscillator. The *ZPE* and *S* of species on Pd(111) were used for Cu(111) and Ag(111). Due to the small differences in energetics relevant to the major conclusions of this study, we calculated *ZPE* and *S* for all intermediates on Cu(111) along the reaction pathway between NO_3* and NO*. The Pd(111) values were used for intermediates after Cu(111), as the conclusions of this study were not sensitive to fine differences in those values. *ZPE* and *S* were calculated separately for Ag(211) due to the different surface geometry. Free energies of all adsorbed states were calculated relative to the free energies of NO_3^-(l), H_2O(g) and H_2(g), and the total energy of the clean slab. For example, for adsorbed NOH*,

$$G_{\mathrm{NOH}^*} = (E_{\mathrm{NOH}^*} + ZPE_{\mathrm{NOH}^*} - TS_{\mathrm{NOH}^*}) - E_{\mathrm{slab}} - G_{\mathrm{NO_3-(l)}} + 2G_{\mathrm{H_2O(g)}} - \frac{5}{2}G_{\mathrm{H_2(g)}}$$

where E_{NOH^*} is the total energy of the adsorbed NOH* on the slab, and E_{slab} is the total energy of the clean slab. The free energy of the nitrate ion in the aqueous phase (NO_3^-(l)) was calculated based on a relevant previous study and was used as a reference state in reaction energetics.[11] Given that difference of adsorption energies of NO_3 with respect to HNO_3(g) and H_2(g) between PW91 used in our study and PBE used in the previous study was less than 0.1 eV, we applied the same extent of correction (+1.12 eV) to HNO_3(g) in this study. Activation energies were calculated using the CI-NEB method with a force cutoff of 0.02 eV $Å^{-1}$.[12] All transition states were verified by confirming the presence of a single imaginary vibrational mode.

The effects of applied electrochemical potential were computed using the computational hydrogen electrode developed by Nørskov and coworkers.[13] The reversible hydrogen electrode (RHE) was set as the electrochemical reference, with hydrogen gas in equilibrium with protons and electrons at a defined potential of 0.00_{RHE}. The free energy change of electrochemical steps was therefore calculated as $\Delta G = \Delta E + \Delta ZPE - T\Delta S + |e|U$, where e is the absolute charge of an electron, and U is the operating potential versus the RHE. Therefore, a more negative operating potential enhances the proton-electron transfer of electrochemical reduction steps. We note that only the free energies of electrochemical steps [*i.e.*, those involving the transfer of a proton-electron (H^+ - e^-) pair] are corrected for potential effects; the energetics of N–O bond breaking effects occurring without concerted proton-electron (H^+ - e^-) transfer are unaffected. The values reported in reference to the Ag/AgCl electrode were calculated by shifting the potential *vs.* RHE (the typical reference for the computational hydrogen electrode) according to the difference in standard reduction potentials. Potentials (E) versus Ag/AgCl in saturated KCl relative to those calculated *vs.* RHE were therefore calculated by:

$$E_{\mathrm{Ag/AgCl}} = E_{\mathrm{RHE}} - 0.197\ \mathrm{V} - 0.059\ \mathrm{V} \times \mathrm{pH}$$

5. Quantification methods

5.1 Quantification of NO_3^- and NO_2^-

NO_3^- and NO_2^- were analyzed by **High-Performance Liquid Chromatography (HPLC)**[14-15] (Agilent Technologies, 1260 Infinity II LC System) equipped with a variable wavelength detector (Agilent 1260 Infinity Variable Wavelength Detector VL). The wavelength of 213 nm was used for detection. A C18 HPLC column (Gemini® 3 µm, 110 Å, 100 × 3 mm) was used for analysis at 25 °C with a binary gradient pumping method to drive mobile phase at 0.4 mL min^{-1}. The mobile phase consisted of 0.01 M *n*-Octylamine in a mixed solution containing 30 vol% of methanol and 70 vol% of DI water, and the pH of the mobile phase was adjusted to 7.0 with H_3PO_4. The running time was 30 min for each sample, and the retention time for NO_3^- and NO_2^- was around 18 and 16 min, respectively. The calibration solutions for NO_3^- or NO_2^- were prepared with KNO_3 and KNO_2 in the concentration range of 0.0625–2 mM (**Figure S6**).

NO_2^- at lower concentrations was determined by **colorimetry** based on the Griess reaction. Two reagents were prepared and stored at 4 ℃, including a) solution A, containing 10 mg mL^{-1} of sulfanilamide and 1.2 M HCl; and b) solution B, containing 1.0 mg mL^{-1} of *N*-(1-Naphthyl)ethylenediamine dihydrochloride (NED). Specifically, the coloring reagent was prepared by mixing equal volumes of solutions A and B. 0.6 mL of the coloring reagent was then mixed with 4 mL of the neutralized sample solution at room temperature. The absorbance measurement was performed on a UV-Vis spectrophotometer (Shimadzu UV-2700) at a wavelength of 540 nm after 15 min of color development. The calibration curve (**Figure S5**) was established by testing a series of standard NO_2^- solutions in the concentration range of 2.7–65.2 µM.

5.2 Quantification of H_2 and N_2

The produced **H_2 and N_2 from the electrochemical** reactor were analyzed by an **on-line GC** (SRI Instruments, 8610C, Multiple Gas #3) equipped with HayeSep D and MolSieve 5Å columns. A thermal conductivity detector was used to detect H_2 and N_2. The calibration curves for H_2 (10–10,000 ppm, Cal Gas Direct) and N_2 (100–100,000 ppm, Shop Cross) were established by analyzing the calibration gases.

To quantify the generated H_2 during the NO3RR measurements, the GC program was started at 2 min after NO3RR was initiated. A 12.5-min programmed cycle was repeated, including 8 min of the GC running period and 4.5 min of the cooling period. For each cycle, the rate of H_2 generation (r, mol s^{-1}) was calculated by

$$r = c \times 10^{-6} \times \frac{p\dot{V} \times 10^{-6} \div 60}{RT}$$

where c is the H_2 content (ppm); $\dot{V}$ is the volumetric flow rate of the inlet gas (12.5 mL min^{-1}); p is the atmospheric pressure (p = 1.013 × 10^5 Pa); R is the gas constant (R = 8.314 J mol^{-1} K^{-1}); T is the room temperature (293.15 K). The total amount of H_2 production (mol) was

calculated by integrating the plot of H_2 production rate (mol s^{-1}) *vs.* reaction time (s) with polynomial curve fitting.

We also examined **N_2 from catalytic NO_2^- reduction** using **on-line GC**. The experiment was carried out as described in catalytic measurements with a lower feeding rate of H_2 (14.5 mL min^{-1}) and CO_2 (2.5 ml min^{-1}), and a higher NO_2^- concentration (0.5 M) to ensure the signal of N_2 was detectable by GC. The total reaction time was 2 h. To quantify the generated N_2, the GC program was started at 5 min after the catalytic reduction was initiated. An 8-min programmed cycle was repeated, including 6 min of the GC running period and 2 min of the cooling period. 15 GC runs were performed in total during the reaction. We considered the consumption of feeding gases (H_2 and CO_2) and generation of N_2 during the reduction of NO_2^- ($2NO_2^- + 3H_2 + 2CO_2 \rightarrow N_2 + 2HCO_3^- + 2H_2O$), which results in a **non-negligible decrease in the flow rate of the gas mixture**. The **net consumption rate of gas** (mL min^{-1}) was calculated by

$$\text{Net consumption rate} = \frac{3+2-1}{2} \times (n_0 - n) \times \frac{RT}{p} \times 10^6 \div \frac{t}{60}$$

where n_0 is the initial amount of NO_2^- (mol); n is the amount of NO_2^- after the reaction (mol); t is the reaction time (s). The calibrated flow rate of the GC inlet gas ($\dot{V}'$) was then obtained by subtracting the net consumption rate from the total feeding rate of H_2 and CO_2 into the reactor. Other steps for calculating the N_2 production were the same as for H_2.

5.3 Quantification of NO_2 and NO

The total concentration of **NO_2 and NO** in the outlet gas of the reactor was tested by **nitrogen oxides detector tubes** (Kitagawa America, No. 175U) with a measuring range of 1–60 ppm. Gas was sampled by an aspirating pump (Kitagawa America, AP-20), and the content of total NO_2 and NO was obtained by reading the scale of the maximum point of the purple stained layer, where the colorimetric reaction occurs in the presence of NO_2 or NO:

$$NO + CrO_3 + H_2SO_4 \longrightarrow NO_2$$

$$NO_2 + \text{3,3'-Dimethylnaphithidine} \longrightarrow \text{Nitroso-compound (pale purple)}$$

5.4 Quantification of N_2O

The concentration of **N_2O** in the outlet gas of the reactor was analyzed by an **off-line GC** equipped with an electron capture detector. The calibration curve of N_2O was established by testing the standard gases in the range of 0.1–300 ppm. The outlet gas from the reactor was collected in sample bags (FlexFoil PLUS, SKC, Inc) and injected into GC for analysis.

5.5 Quantification of NH_4^+

NH_4^+ was quantified by **indophenol blue colorimetry**.[15-16] Three reagents were prepared, including a) coloring solution, containing 0.4 M sodium salicylate and 0.32 M NaOH; b) oxidizing solution, containing 0.75 M NaOH in NaClO solution (available chlorine: 4.00–4.99%); and c) catalyst solution, containing 10 mg mL^{-1} of $Na_2[Fe(CN)_5NO]\cdot 2H_2O$. Specifically, 50 μL of the

oxidizing solution, 500 μL of the coloring solution, and 50 μL of the catalyst solution were added sequentially into 4 mL of the testing sample, followed by ultrasonication for 10 s to mix the reagents. The absorbance measurement was performed on a UV-Vis spectrophotometer (Shimadzu UV-2700) at a wavelength of 665 nm after 2 h of color development. The calibration curves (**Figure S5**) were established by examining a series of standard NH_4^+ solutions in the concentration range of 5–300 μM. It should be noted that NH_4^+ quantification by colorimetry is pH-sensitive. Therefore, multiple calibration curves were prepared according to the specific composition of the sample solutions. For the CO_2-saturated solutions, the pH was adjusted to 13 by adding KOH before the colorimetric test.

5.6 Quantification of NH_2OH

NH_2OH was determined by a **colorimetric method.**[17] 1 mL of the sample solution, 1 mL of 0.05 M phosphate buffer solution (pH = 6.8), 0.8 mL of DI water, 0.2 mL of trichloroacetic acid, 1 mL of 8-quinolinol, and 1 mL of 1 M Na_2CO_3 solution were mixed and placed in a boiling water bath for 1 min for color development. The solution was then removed from the water bath and cooled at room temperature for 15 min. The absorbance was measured at 705 nm on a UV-Vis spectrophotometer. The calibration curve (**Figure S5**) was established by testing a series of NH_2OH solutions in the concentration range of 6–40 μM.

5.7 Quantification of $^{14}NH_4^+$ and $^{15}NH_4^+$

$^{14}NH_4^+$ and $^{15}NH_4^+$ were quantified by **^{1}H nuclear magnetic resonance (NMR) spectroscopy** obtained on a Bruker Avance III 600 Spectrometer. Samples were prepared by properly diluting the electrolyte with a solution containing 0.1 M H_2SO_4 and 0.1 M KCl, and then mixing 0.8 mL of the diluted solution with 0.2 mL of DMSO-d_6. Calibration curves were established by testing a series of solutions containing $^{14}NH_4^+$ and $^{15}NH_4^+$ in 0.1 M H_2SO_4 and 0.1 M KCl with concentrations ranging from 5 to 80 μM (**Figure S7**). The scan number was 2,048. Water suppression was performed for all NMR measurements.

6. Materials characterization

6.1 Physical characterization

To physical characterization of materials, X-ray diffraction (XRD) crystallography was carried out on a Siemens D500 X-ray diffractometer with a Cu Kα source (λ = 1.5418 Å) at a tube voltage of 45 kV and a tube current of 30 mA. The scan was performed at a rate of 10° min^{-1} and a step size of 0.01°. X-ray photoelectron spectroscopy (XPS) was carried out on a Kratos Amicus/ESCA 3400 X-ray photoelectron spectrometer with Mg Kα X-ray (1,253.7 eV). All spectra were calibrated with the C 1s peak at 284.8 eV. Scanning electron microscopy (SEM) was performed on a FEI Quanta-250 field-emission scanning electron microscope. Inductively coupled plasma-optical emission spectroscopy (ICP-OES) was performed on a PerkinElmer® Optima™ 8000 ICP-OES instrument. The calibration in the range of 0.6–100 ppb was established by diluting the standard Ag^+ solution (1,000 μg mL^{-1}, Inorganic Ventures) with 5% v/v nitric acid.

6.2 Determination of the electrochemical active surface area (ECSA)

The electrochemical active surface area (ECSA) of the Ag electrodes (OD-Ag, Ag foil, and Ag NPs/Ag) was measured by underpotential deposition (UPD) of Pb.[18] Cyclic voltammetry (CV) was conducted in a three-electrode system with an electrolyte consisting of 5 mM $Pb(NO_3)_2$, 10 mM HNO_3, and 10 mM KCl between −0.10 and −0.48 $V_{Ag/AgCl}$ with a scan rate of 10 mV s^{-1}. The peak for monolayer UPD of Pb was used for ECSA calculation, which corresponds to a charge of 1.67×10^{-3} cm^2 μC^{-1}.

6.3 Determination of the active surface area of Pd

The active surface area of Pd for Pd/C was measured by H_2 pulse chemisorption on an AutoChem II 2920 chemisorption analyzer. The catalyst was first reduced at 200 ℃ (10 ℃ min^{-1} ramp rate) under a flow of 10% H_2/Ar (50 mL min^{-1}) for 1 h. Then, a 1-hour purging step was carried out with Ar (20 mL min^{-1}) at 200 ℃ before the catalyst was cooled to 35 ℃. After the baseline signal from the thermal conductivity detector was stable, a series of pulse streams of 10% H_2-Ar was injected until the injected gas volume emerged from the sample tube was unchanged and the detected peak integral was constant. The stoichiometric factor for H_2 adsorption was assumed to be 2 (one H_2 molecule for two Pd atoms).[19]

Supplementary Figures (1–33)

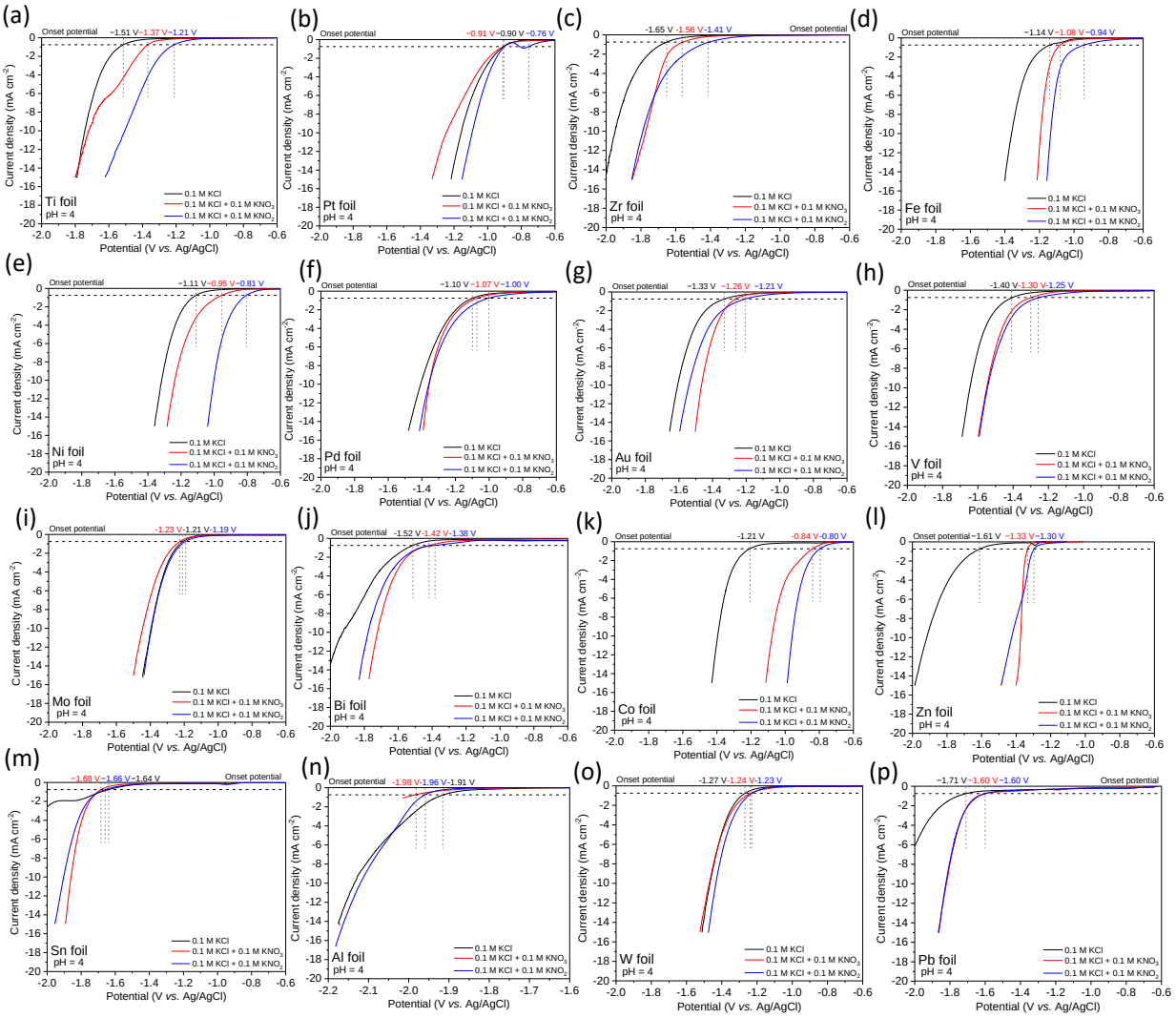

Figure S1. Linear sweep voltammograms of metal foil electrodes. (a)–(p) correspond to the voltammograms Ti, Pt, Zr, Fe, Ni, Pd, Au, V, Mo, Bi, Co, Zn, Sn, Al, W, and Pb in three different solutions: 0.1 M KCl (black curves), 0.1 M KCl with 0.1 M NO_3^- (red curves), and 0.1 M KCl with 0.1 M NO_2^- (blue curves). The onset potentials (defined as the potential at −0.75 mA cm^{-2}) of NO_3^- reduction, NO_2^- reduction, and HER are labeled on the top of each graph. The geometric area of the electrodes was 4 cm^2. The range of *x*-axis in Figure S 1n (Al foil) is from −1.6 to −2.2 $V_{Ag/AgCl}$.

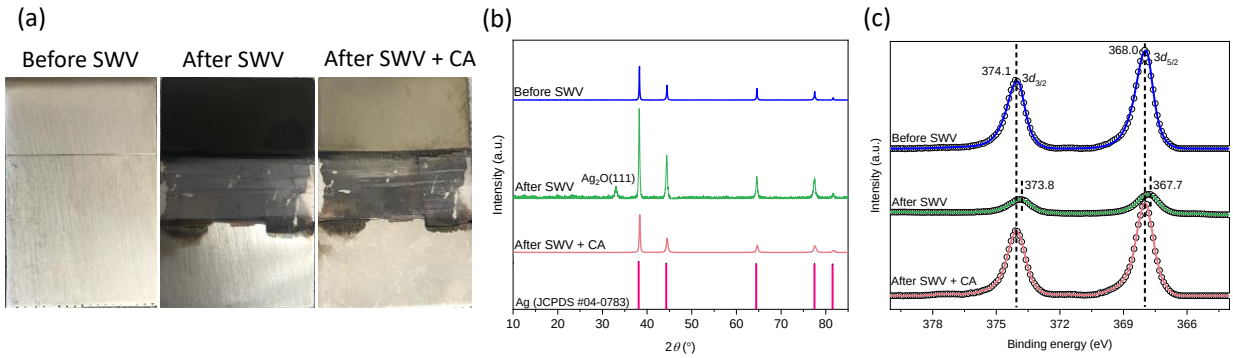

Figure S2. Characterization of Ag foil during the preparation of OD-Ag. (a) Photographs. (b) XRD patterns. (c) XPS Ag 3*d* spectra. The surface color of Ag foil was observed to periodically change between white and black during the SWV operation, while a yellow surface was finally obtained after the CA operation. These black and yellow layers were OD-AgO_x and OD-Ag, respectively. XRD confirms the mono-constituent Ag^0 in the prepared OD-Ag (same as Ag foil), in comparison to OD-AgO_x possessing the characteristic diffraction plane of $Ag_2O(111)$ at 32.8°. XPS exhibited a negative shift of 0.3 eV in the binding energy of both Ag 3d peaks ($3d_{3/2}$ and $3d_{5/2}$) for OD-AgO_x as compared to Ag foil and OD-Ag. In addition, OD-AgO_x has much lower Ag 3d peak intensity than Ag foil and OD-Ag, because of the higher coverage of oxygen atoms on surface.

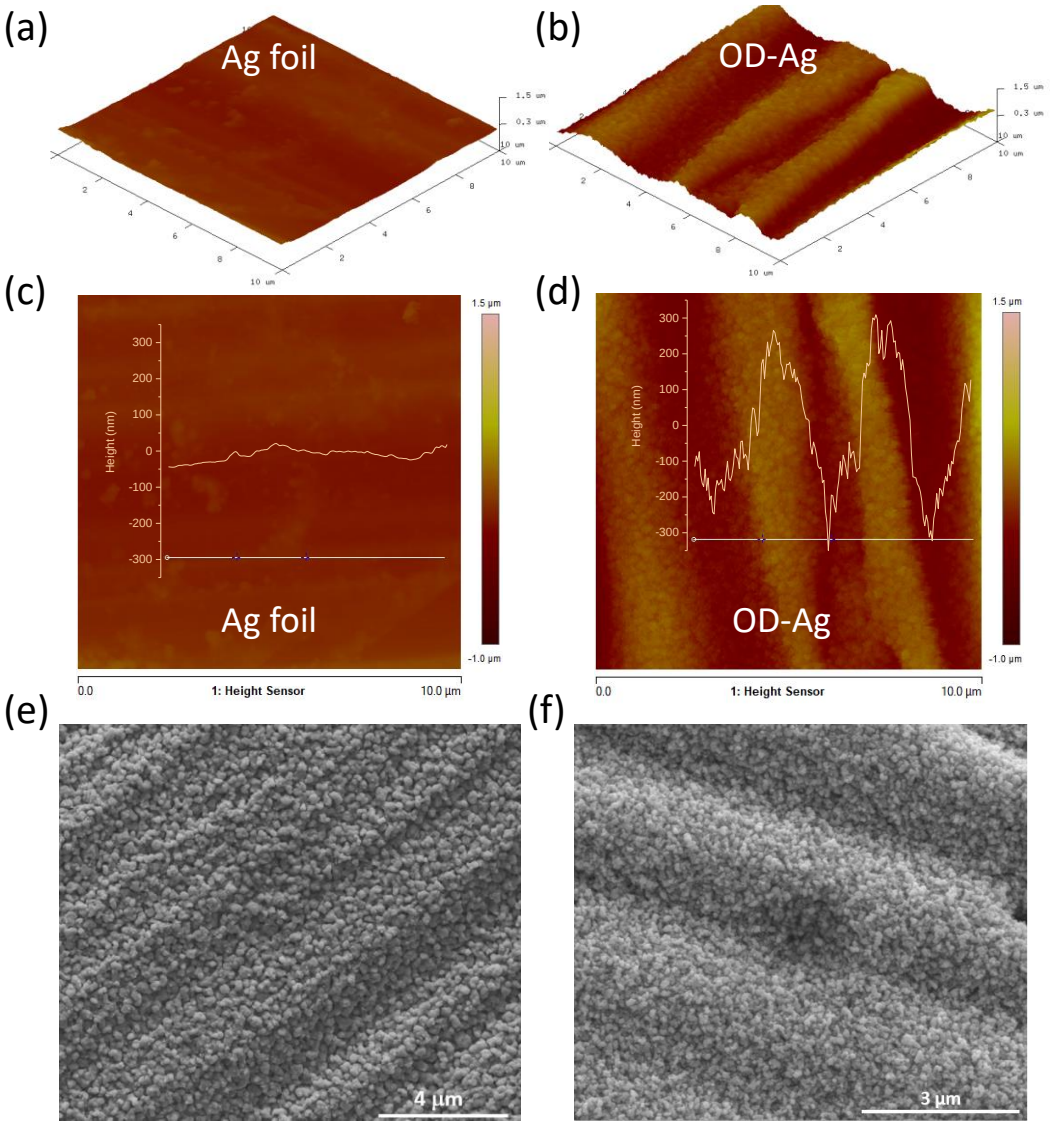

Figure S3. Characterization of the surface morphology of OD-Ag. (a) – (b) AFM 3D images of Ag foil and OD-Ag. (c) – (d) AFM 2D images of Ag foil and OD-Ag with a 7-µm section height profile graph inserted. (e) – (f) Low-magnification SEM images of OD-Ag.

(a)

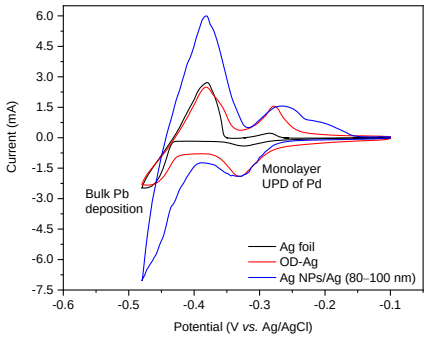

(b)

Material	Preparation condition	Geometric area (cm^2)	ECSA (cm^2)
Ag foil	N/A	2	2.1
Ag NPs/Ag (80–100 nm)	Spray-coating	2	25.9
OD-Ag	SWV + CA	2	27.1

Figure S4. Measurement of ECSA for the Ag electrodes. (a) Cyclic voltammograms of Ag foil, OD-Ag, and Ag NPs/Ag in the electrolyte consisting of 5 mM $Pb(NO_3)_2$, 10 mM HNO_3, and 10 mM KCl. The scan rate was 10 mV s^{-1}. The peak for monolayer UPD of Pb was used for ECSA calculation, which corresponds to a charge of 1.67×10^{-3} cm^2 μC^{-1}.[18] (b) Summary of ECSA of the Ag electrodes.

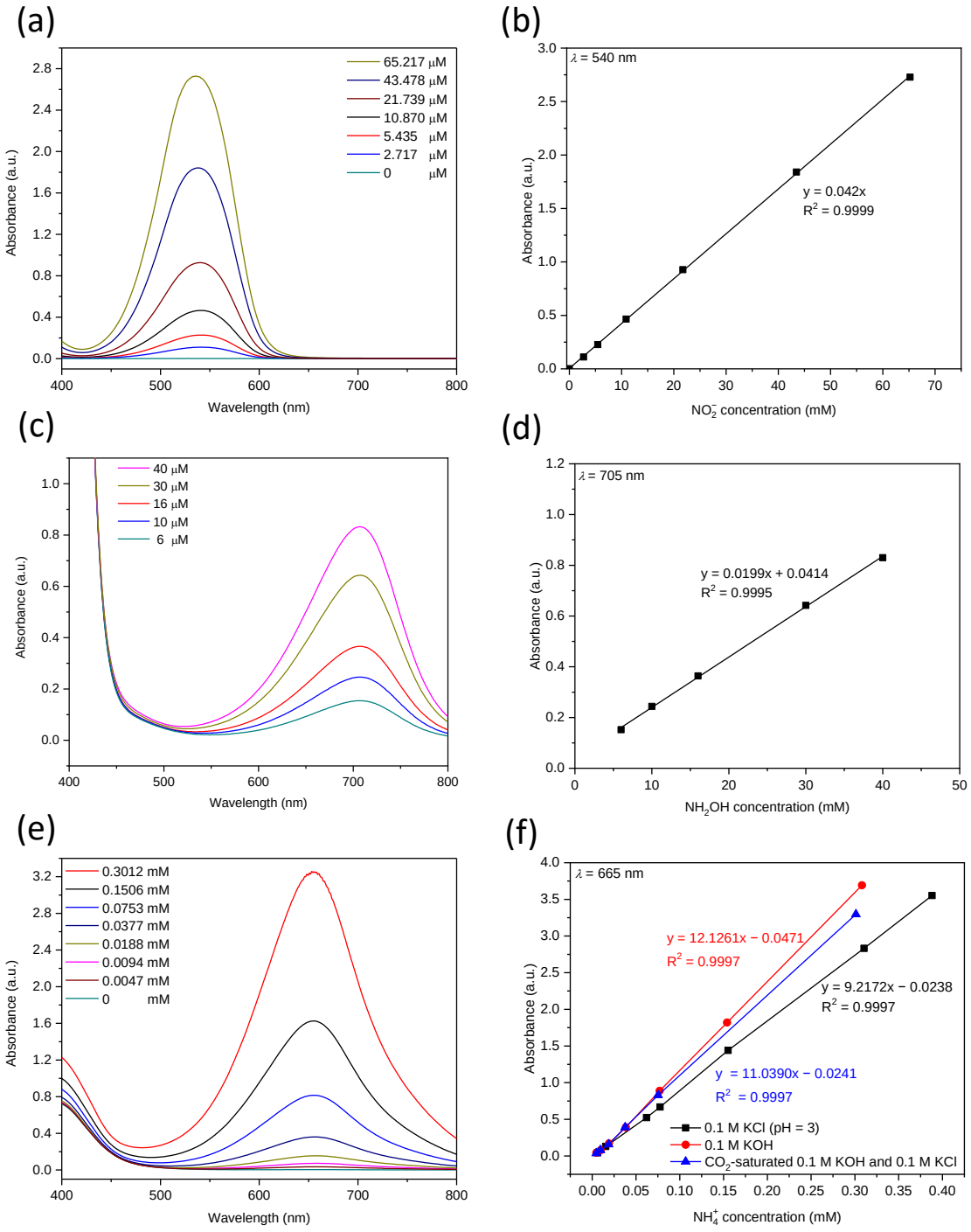

Figure S5. UV-Vis calibrations of NO_2^-, NH_2OH, and NH_4^+. (a) – (b) UV-Vis spectra and calibration curve of standard NO_2^- solutions. (c) – (d) UV-Vis spectra and calibration curve of standard NH_2OH solutions. (e) UV-Vis spectra of the standard NH_4^+ solutions in CO_2-saturated 0.1 M KOH and 0.1 M KCl. The pH of the sample solutions was adjusted to 13 by adding KOH before the colorimetric test. (f) Calibration curves for standard NH_4^+ solutions in different media.

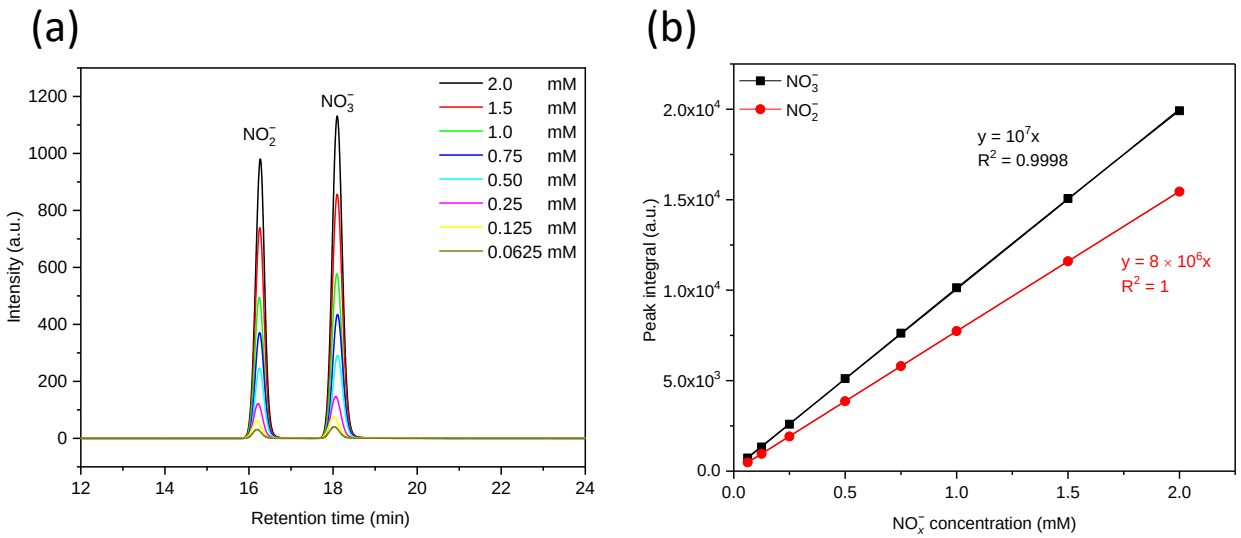

Figure S6. HPLC calibration with standard NO_3^- and NO_2^- solutions. (a) HPLC graphs. The retention time was around 16 or 18 min for NO_2^- or NO_3^-, respectively. (b) Calibration curves.

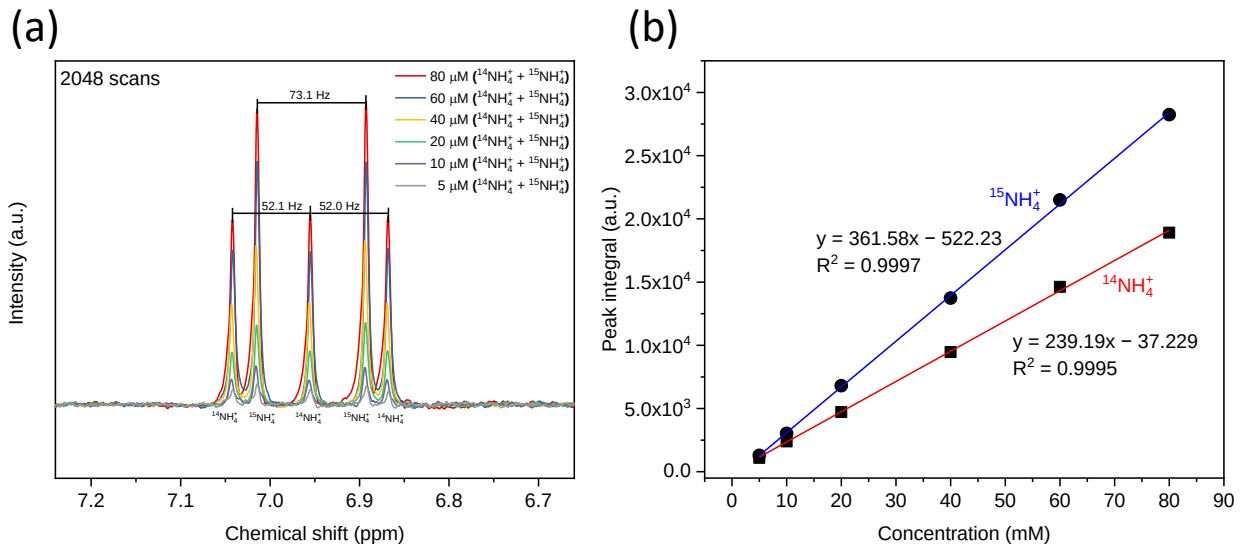

Figure S7. ^{1}H NMR calibration with solutions containing $^{14}NH_4^+$ and $^{15}NH_4^+$ (in 0.1 M KCl with 0.1 M H_2SO_4). (a) ^{1}H NMR spectra collected with 2,048 scans. (b) Calibration curves of $^{14}NH_4^+$ and $^{15}NH_4^+$.

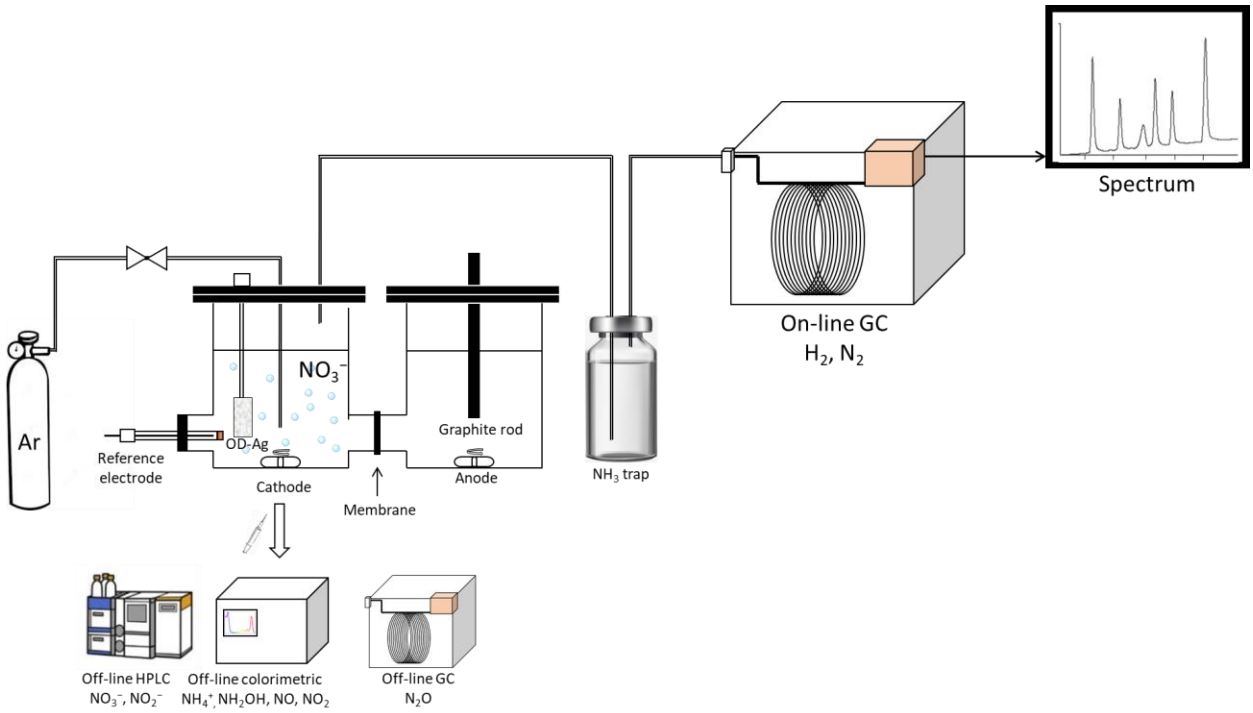

Figure S8. The experimental setup for NO3RR measurements. The setup includes the H-type cell, NH_3 trapping solution, on-line GC for H_2 and N_2 quantification, and off-line quantification of NO_3^-, NO_2^-, NH_4^+, NH_2OH, NO_2, NO, and N_2O.

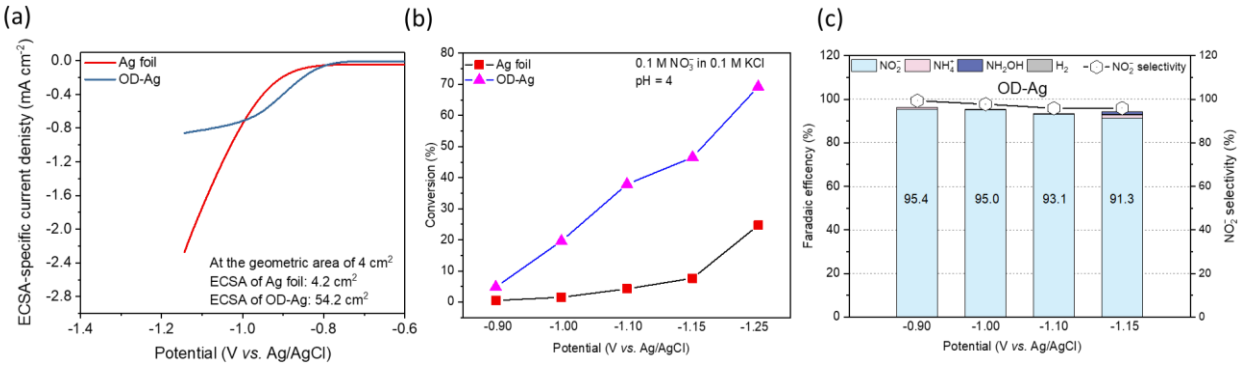

Figure S9. NO3RR in 0.1 M KCl (pH = 4) with 0.1 M NO_3^-. The geometric area of all electrodes was 4 cm^2. (a) ECSA-specific LSV on Ag foil (red curve) and OD-Ag (blue curve) in 0.1 M KCl with 0.1 M NO_3^- at pH 4. The ECSA for Ag foil and OD-Ag were 4.2 and 54.2 cm^2, respectively. (b) Conversion of NO_3^- on Ag foil and OD-Ag for 1-hour electrolysis at different potential. (c) FE and NO_2^- selectivity on OD-Ag for 1-hour electrolysis at different potential.

As shown in **Figure S9a**, the ECSA-specific current density for OD-Ag has outperformed Ag foil in the potential range ocf −0.8 to −1.0 V. Under potentials more negative than −1.0 V, the reaction on OD-Ag is more likely to be limited by the mass transport due to its large surface area (ECSA of OD-Ag *vs.* Ag foil: 54.2 *vs.* 4.2 cm^2, at the geometric area of 4 cm^2). LSV is a transient potential sweep process carried out without the magnetic stirring of electrolyte, and thus mass transport of both reactant supply and product giveaway becomes limited due to large current demand under potentials more negative than −1.0 V.

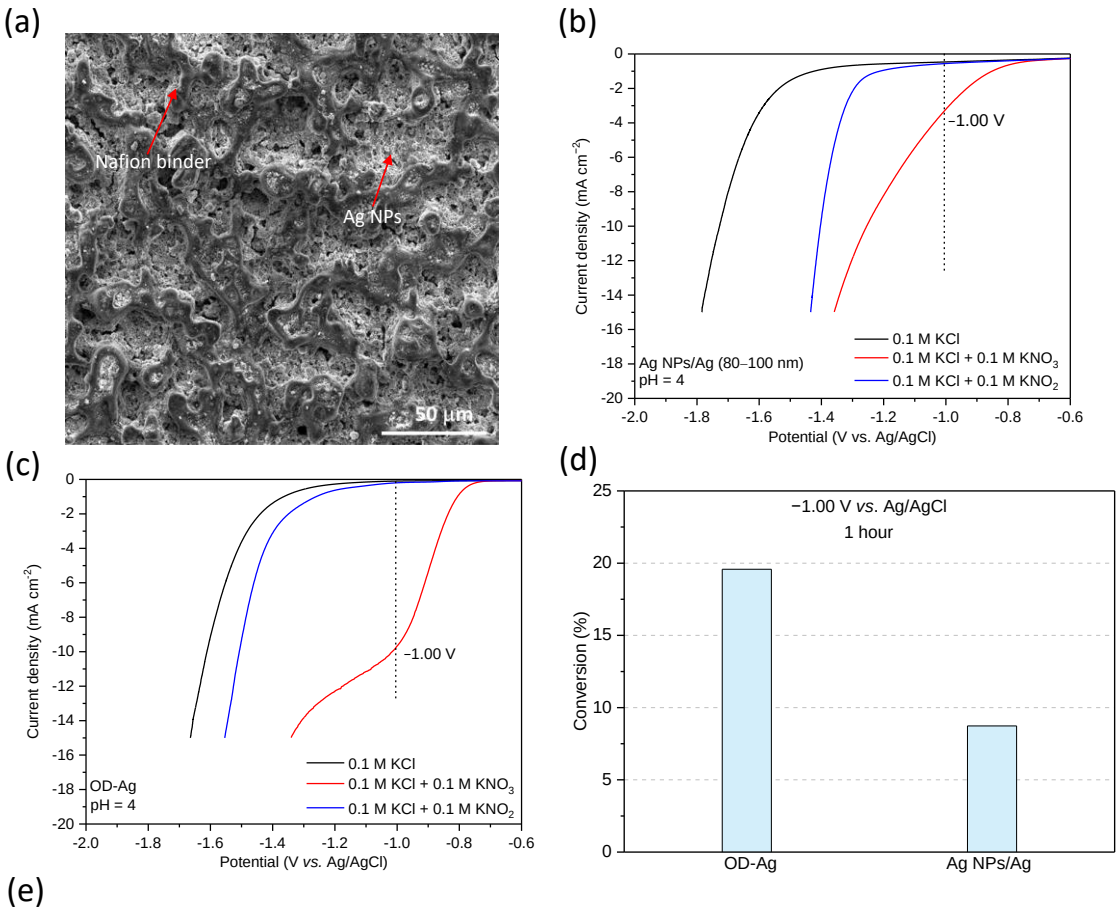

Electrode	Geometric area (cm^2)	ECSA (cm^2)	Current @−1.00 V (mA)	ECSA-specific current density (mA cm^{-2})
Ag NPs/Ag (80-100nm)	4	51.80	−13.44	0.26
OD-Ag	4	54.20	−38.80	0.72

Figure S10. Comparison of OD-Ag and Ag NPs/Ag (80–100 nm, loading of 1.5 mg_{Ag} cm^{-2}. (a) SEM image of Ag NPs/Ag (with Nafion as the binder). (b) – (c) Linear sweep voltammograms in 0.1 M KCl, 0.1 M KCl with 0.1 M NO_3^-, and 0.1 M KCl with 0.1 M NO_2^-, respectively. (d) NO_3^- conversion in 0.1 M KCl (pH = 4) with 0.1 M NO_3^- at −1.00 $V_{Ag/AgCl}$ for 1 h. (e) Summary of area-specific NO3RR activity). It should be pointed out that both OD-Ag and Ag NPs have a similar average size of Ag particles (~100 nm *vs.* 80–100 nm), very close ESCA (27.1 cm^2 *vs.* 25.9 cm^2, **Figure S4b**), and with the same sized Ag foil (2 cm^2) as electrode substrate.

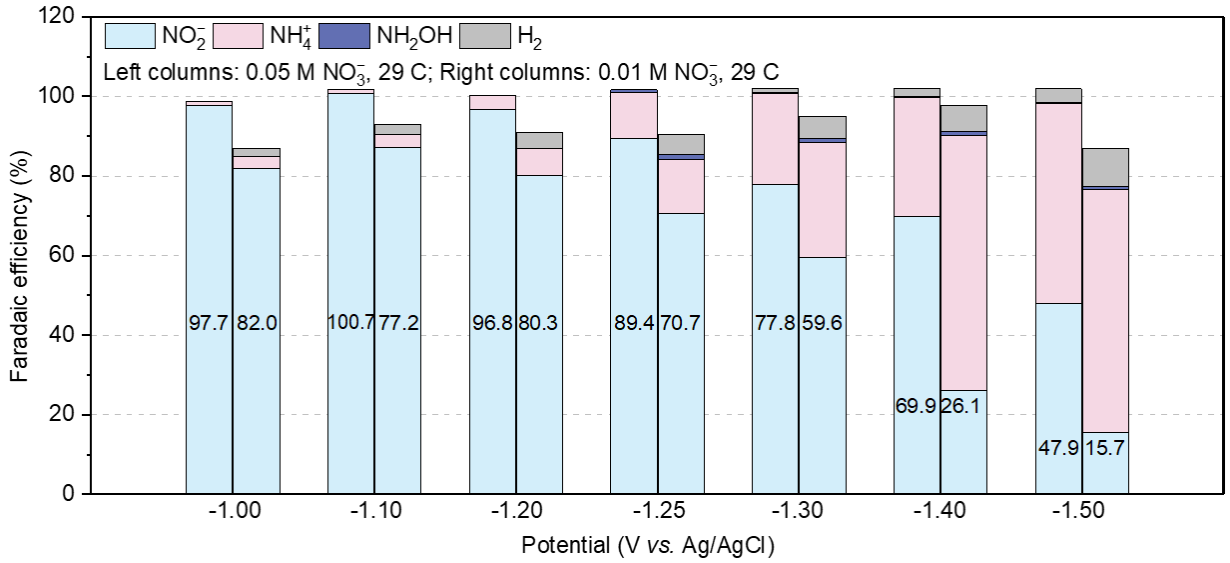

Figure S11. FE of NO3RR on OD-Ag with 0.05 M and 0.01 M NO_3^-. Left columns: 0.05 M NO_3^-. Right columns: 0.01 M NO_3^-. The electrolyte was 0.1 M KCl (pH = 4). The applied charge was 29 C which is the theoretical charge required for NO3RR to NO_2^- in the system. The geometric area of the electrode was 6 cm^2 for −1.00 and −1.10 $V_{Ag/AgCl}$ with 0.01 M NO_3^-, and 2 cm^2 for all other conditions. The error bars represent the standard deviation for at least three independent measurements.

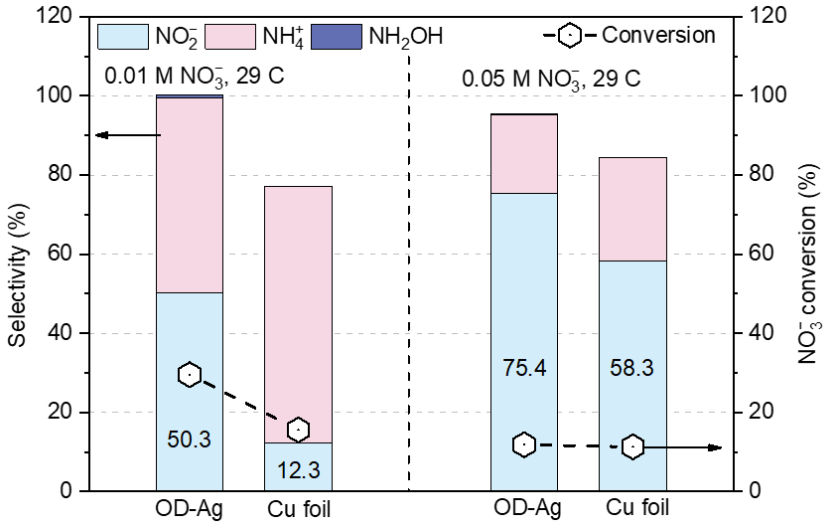

Figure S12. Product selectivity and NO_3^- conversion of NO3RR on OD-Ag and Cu foil at −1.50 $V_{Ag/AgCl}$. The electrolyte was 0.1 M KCl (pH = 4) and the geometric area of the electrodes was 2 cm^2. The applied charge was 29 C.

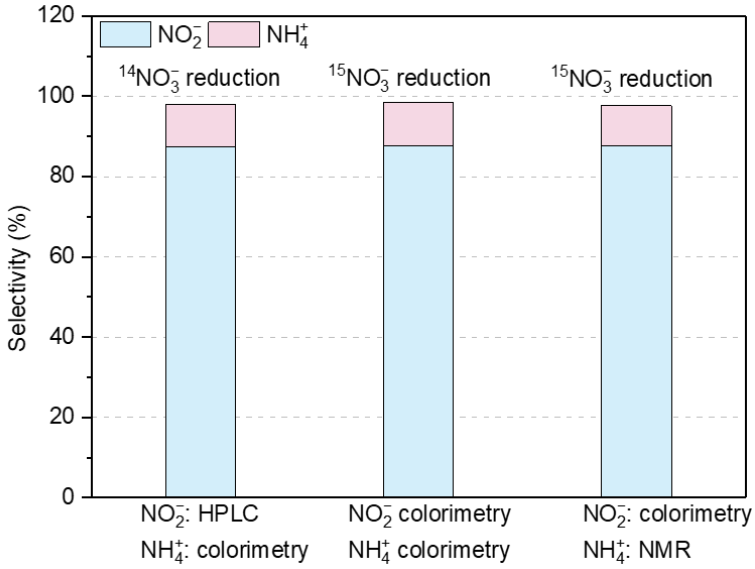

Figure S13. Comparison of different quantification methods. NO3RR was performed in 0.1 M KCl with 0.01 M $^{14}NO_3^-$ or $^{15}NO_3^-$ on OD-Ag. The applied potential was −1.30 $V_{Ag/AgCl}$ and applied charge was 29 C. The produced NO_2^- was quantified by high-performance liquid chromatography (HPLC) or Griess colorimetry, and NH_4^+ was quantified by indophenol blue colorimetry or 1 H NMR.

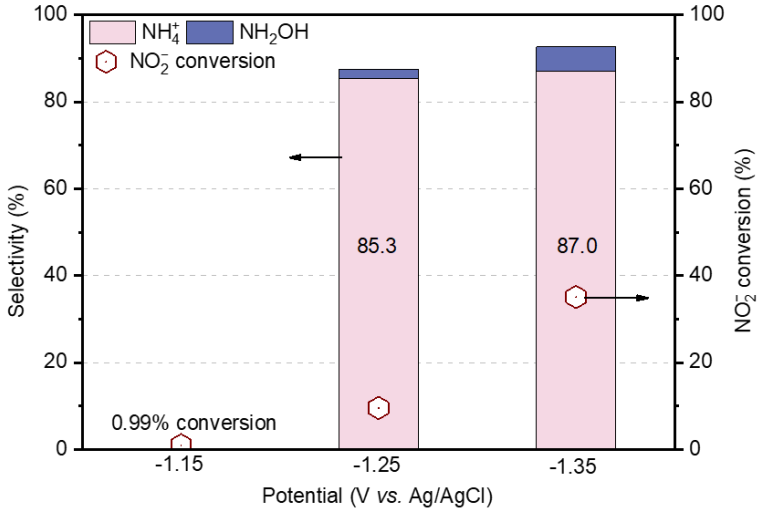

Figure S14. Electrochemical reduction of 0.01 M NO_2^- on OD-Ag. Product selectivity and NO_2^- conversion for 1-hour electrolysis. The electrolyte was 0.1 M KCl (pH = 4) and the geometric area of OD-Ag was 2 cm^2.

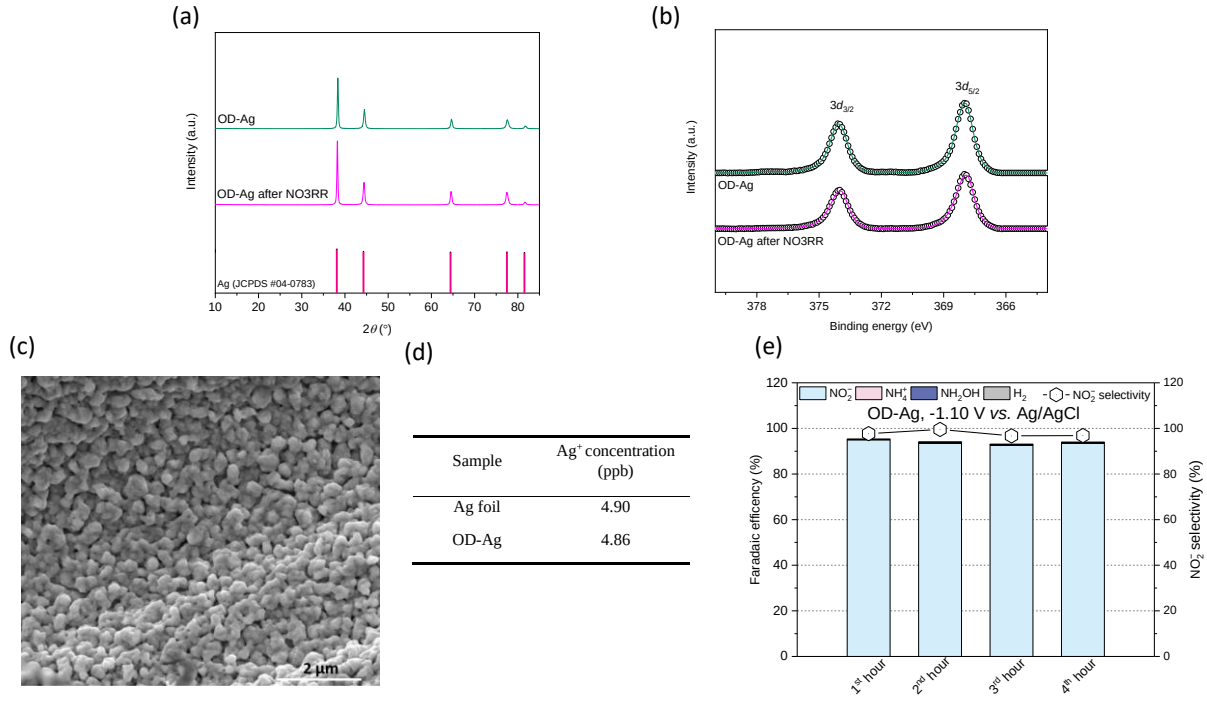

Sample	Ag^+ concentration (ppb)
Ag foil	4.90
OD-Ag	4.86

Figure S15. Stability measurements on OD-Ag (geometric area of 4 cm^2) for NO3RR. Electrolysis was performed in 0.1 M KCl (pH = 4) with 0.1 M NO_3^- at −1.00 $V_{Ag/AgCl}$. (a) XRD patterns, (b) XPS Ag 3*d* spectra, (c) SEM image, and (d) Ag^+ content in the electrolyte by ICP-OES after 1-hour electrolysis. (e) Faradaic efficiency and NO_2^- selectivity for four consecutive 1-hour electrolysis on the same OD-Ag.

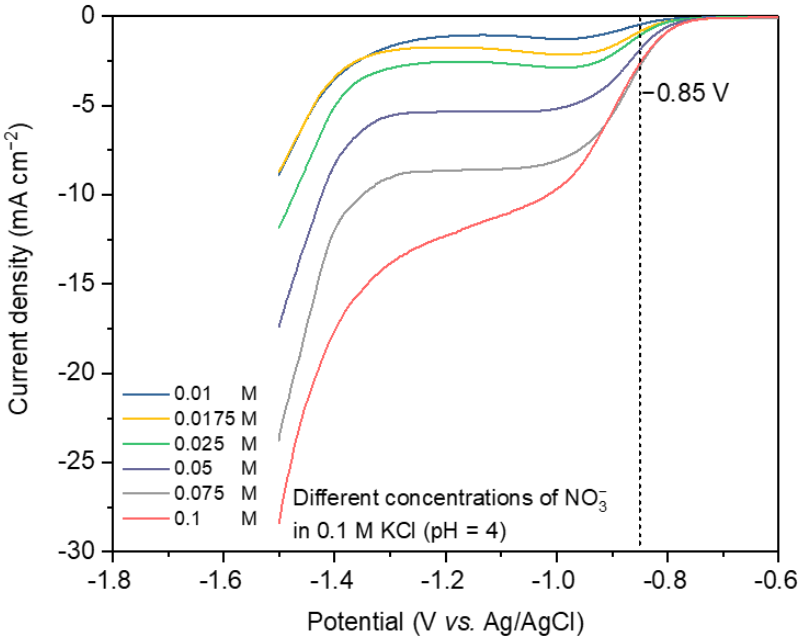

Figure S16. Linear sweep voltammograms of OD-Ag in 0.1 M KCl (pH = 4) with different concentrations of NO_3^-. The geometric area of the electrodes was 4 cm^2.

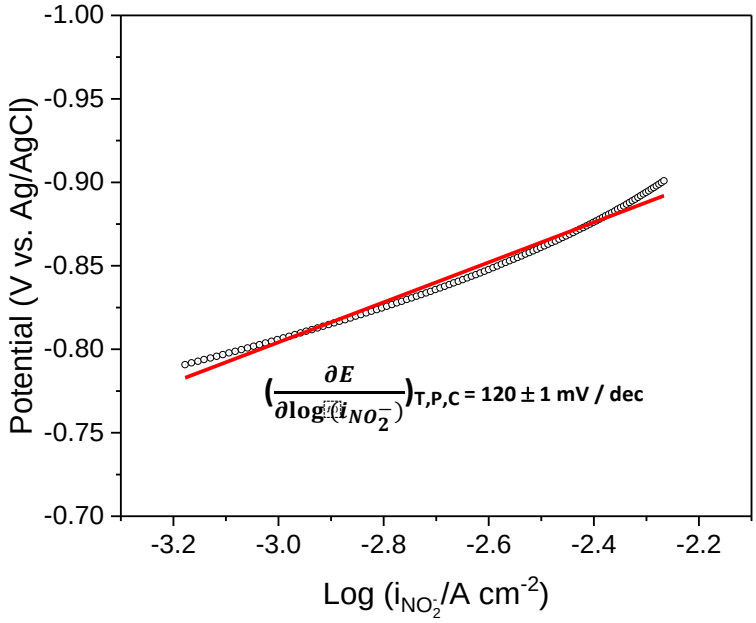

Figure S17. NO_2^- partial current density Tafel plot. The data was obtained from the Linear sweep voltammograms (LSV) with a potential range from −0.79 V (onset potential of NO3RR) to −0.90 $V_{Ag/AgCl}$. LSV was performed on OD-Ag in 0.1 M KCl (pH = 4) with 0.1 M of NO_3^- (as shown in the main text **Figure 2c**). The geometric area of the electrodes was 4 cm^2.

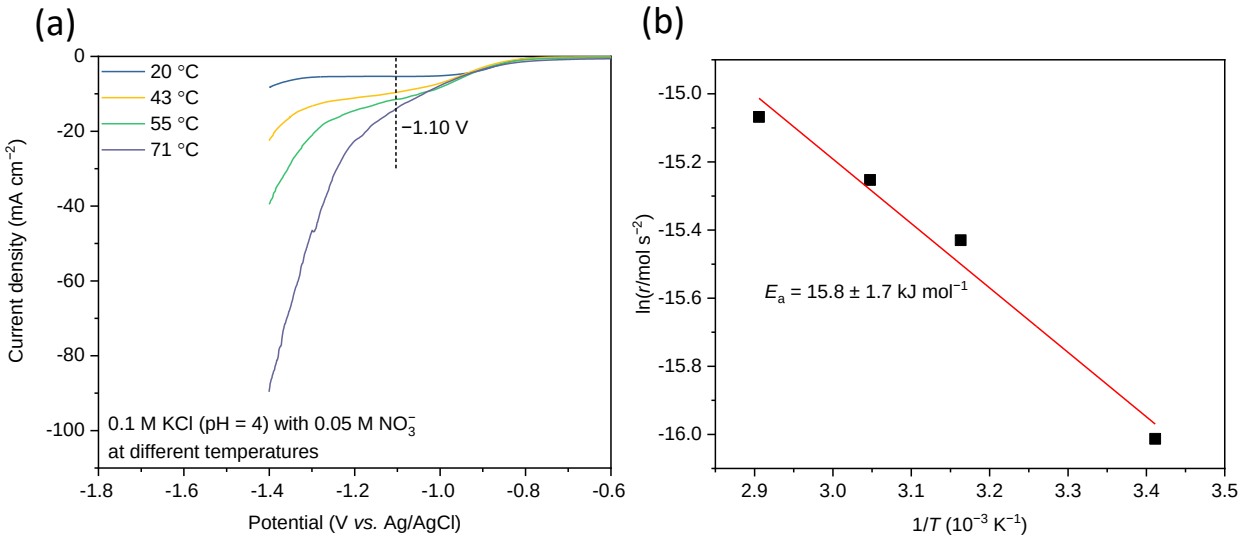

Figure S18. Activation energy for NO3RR on OD-Ag at −1.10 $V_{Ag/AgCl}$. (a) Linear sweep voltammograms of OD-Ag in 0.1 M KCl (pH = 4) with 0.05 M NO_3^- at different temperatures. The geometric area of OD-Ag was 4 cm^2. (b) Arrhenius plot for NO3RR on OD-Ag at −1.10 $V_{Ag/AgCl}$.

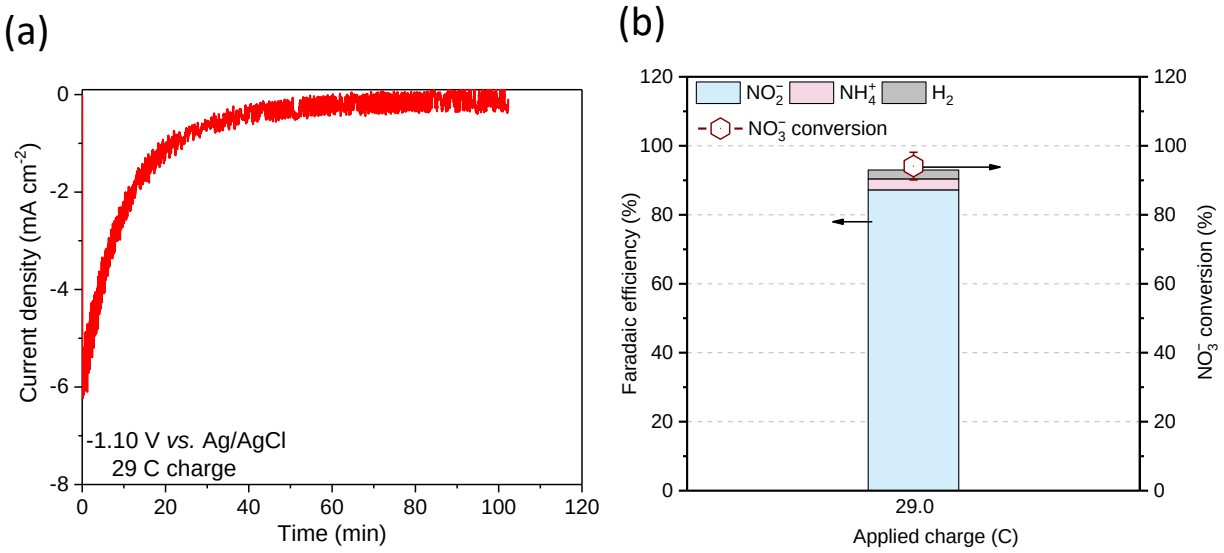

Figure S19. NO3RR on OD-Ag with 29 C applied charge at −1.10 $V_{Ag/AgCl}$. The electrolyte was in 0.1 M KCl (pH = 4) with 0.01 M NO_3^- and the geometric area of OD-Ag was 6 cm^2. (a) Current density-time profile with applying a theoretical charge of 29 C for complete convert 0.01 M NO_3^- to NO_2^-. (b) Faradaic efficiency and NO_3^- conversion. The error bars represent the standard deviations of at least three independent measurements.

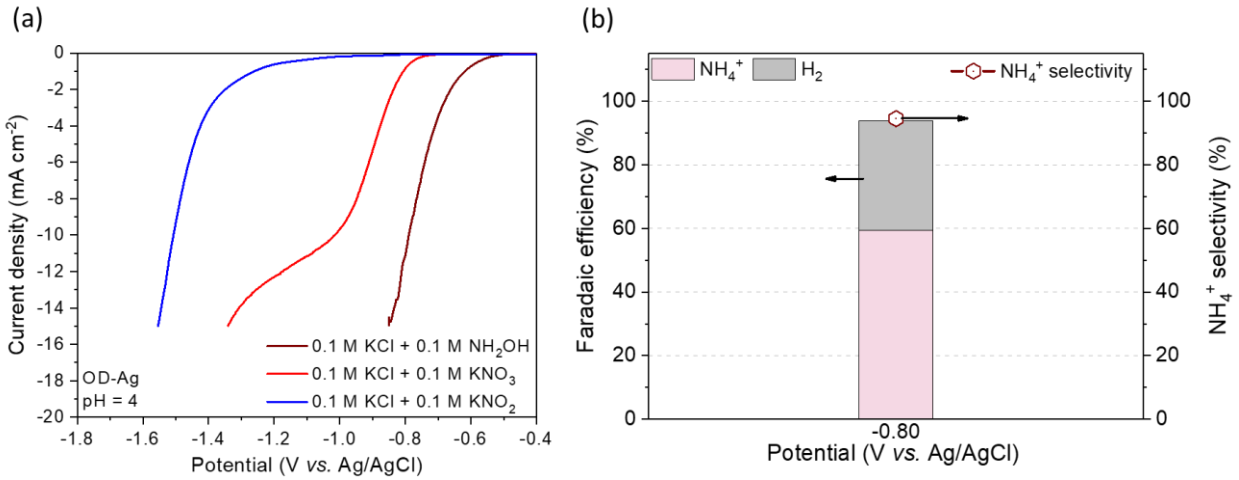

Figure S20. Electrochemical reduction of NH_2OH on OD-Ag (4 cm^2 geometric area) at pH 4. a) Linear sweep voltammetry in 0.1 M KCl with 0.1 M NH_2OH, 0.1 M KNO_3, and 0.1 M KNO_2, respectively. b) FE and NH_4^+ selectivity of electrolysis in 0.1 M KCl with 0.1 M NH_2OH at −0.80 $V_{Ag/AgCl}$ for 1 hour.

Supplementary Note 1. Isotopic experiment and kinetics modeling

The isotopic experiment was conducted in 0.1 M KCl (pH = 4) with 0.025 M $K^{15}NO_3$ and 0.025 M $K^{14}NO_2$. CA was carried out with different applied charges. The N-species in the resulting solution were quantified by HPLC (for $^{15}NO_3^-$), colorimetry (for total $^{14}NO_2^-$ and $^{15}NO_2^-$), and NMR ($^{14}NH_4^+$ and $^{15}NH_4^+$), as detailed in **Experimental Section**.

We consider the following reactions in the electrolytic cell:

$$^{15}NO_3^- \rightarrow {}^{15}NO_2^- \qquad k_1$$

$$^{14}NO_2^- \rightarrow {}^{14}NH_4^+ \qquad k_2$$

$$^{15}NO_3^- \rightarrow {}^{15}NH_4^+ \qquad k_3$$

$$^{15}NO_2^- \rightarrow {}^{15}NH_4^+ \qquad k_4$$

All reactions were assumed to be first-order[20-21] without isotopic effect ($k_2 = k_4$). In addition, 100% ^{15}N and ^{14}N balances were assumed, in light of the ~100% nitrogen balance for the electro-reduction of NO_3^- and NO_2^-, and the low selectivity towards NO_2, NO, N_2O, and NH_2OH (**Figure 2d and Table S3**).

Let A = $^{15}NO_3^-$, B = $^{15}NO_2^-$, C = $^{15}NH_4^+$, b = $^{14}NO_2^-$, and c = $^{14}NH_4^+$. The following 5 equations can be obtained by rate law:

$$\frac{\mathrm{d[A]}}{\mathrm{d}t} = -k_1[\mathrm{A}] - k_3[\mathrm{A}]$$

$$\frac{\mathrm{d[B]}}{\mathrm{d}t} = k_1[\mathrm{A}] - k_2[\mathrm{B}]$$

$$\frac{\mathrm{d[C]}}{\mathrm{d}t} = k_3[\mathrm{A}] + k_2[\mathrm{B}]$$

$$\frac{\mathrm{d[b]}}{\mathrm{d}t} = -k_2[\mathrm{b}]$$

$$\frac{\mathrm{d[c]}}{\mathrm{d}t} = k_2[\mathrm{b}]$$

By using the boundary conditions ([X] = $[X]_0$ for all species at $t = 0$) and N balance ([A] + [B] + [C] = $[A]_0 + [B]_0 + [C]_0$), the solutions for [A], [b], and [B] are:

$$[\mathrm{A}] = [\mathrm{A}]_0 \mathrm{e}^{-(k_1+k_3)t}$$

$$[\mathrm{b}] = [\mathrm{b}]_0 \mathrm{e}^{-k_2 t}$$

$$[\mathrm{B}] = \frac{k_1[\mathrm{A}]_0}{k_2 - k_1 - k_3}\left[\mathrm{e}^{-(k_1+k_3)t} - \mathrm{e}^{-k_2 t}\right] = \mathrm{f}(t)k_1$$

Therefore, k_2 and ($k_1 + k_3$) were calculated by linear regression of $\ln([b]/[b]_0)$ and $\ln([A]/[A]_0)$ on t; k_1 was calculated by linear regression of [B] on $\mathrm{f}(t) = \frac{[\mathrm{A}]_0}{k_2-k_1-k_3}\left[\mathrm{e}^{-(k_1+k_3)t} - \mathrm{e}^{-k_2 t}\right]$. The fitted curves and calculated rate constants are summarized in **Figure S21**.

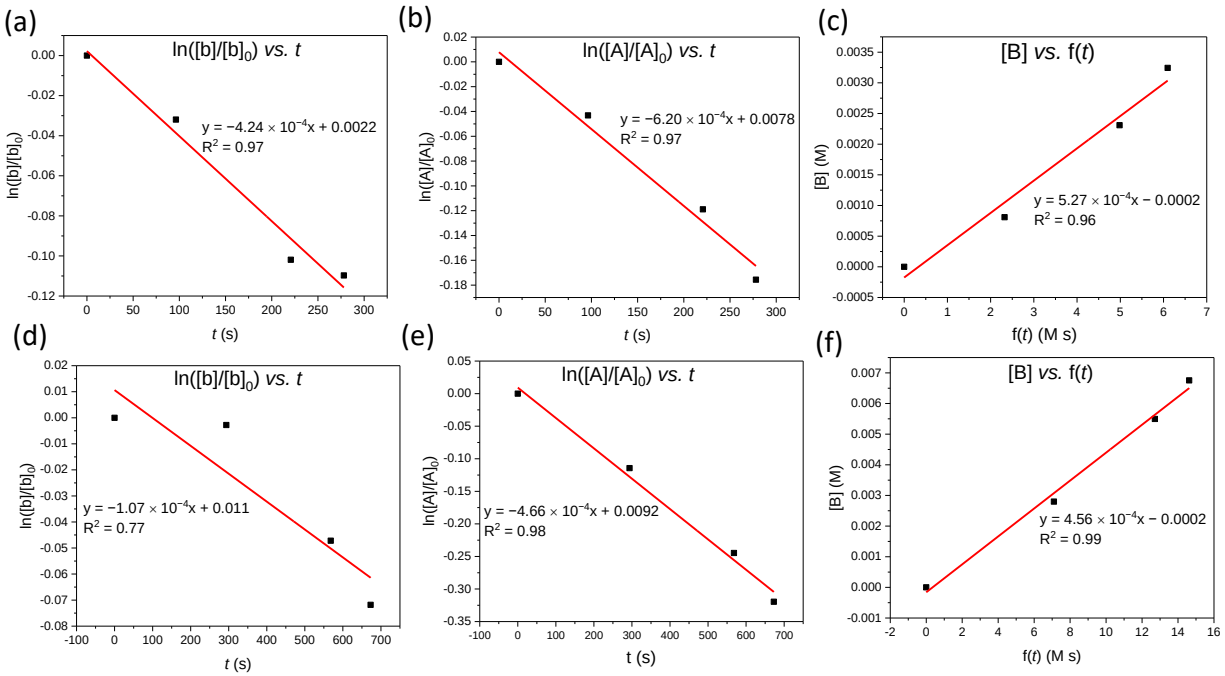

(g)

Potential (V *vs.* Ag/AgCl)	k_1 (min^{-1})	k_2 (min^{-1})	k_3 (min^{-1})	R^2 for k_2	R^2 for (k_1 + k_3)	R^2 for k_1
−1.50	0.0316	0.0255	0.0056	0.97	0.97	0.96
−1.30	0.0273	0.00643	0.0007	0.77	0.98	0.99

Figure S21. Electrolysis with 0.025 M $^{15}NO_3^-$ and 0.025 M $^{14}NO_2^-$. The electrolyte was 0.1 M KCl (pH = 4) and the geometric area of OD-Ag was 2 cm^2. (a)–(c) Electrolysis at −1.50 $V_{Ag/AgCl}$. (d)–(f) Electrolysis at −1.30 $V_{Ag/AgCl}$. (g) Summary of linear regression results.

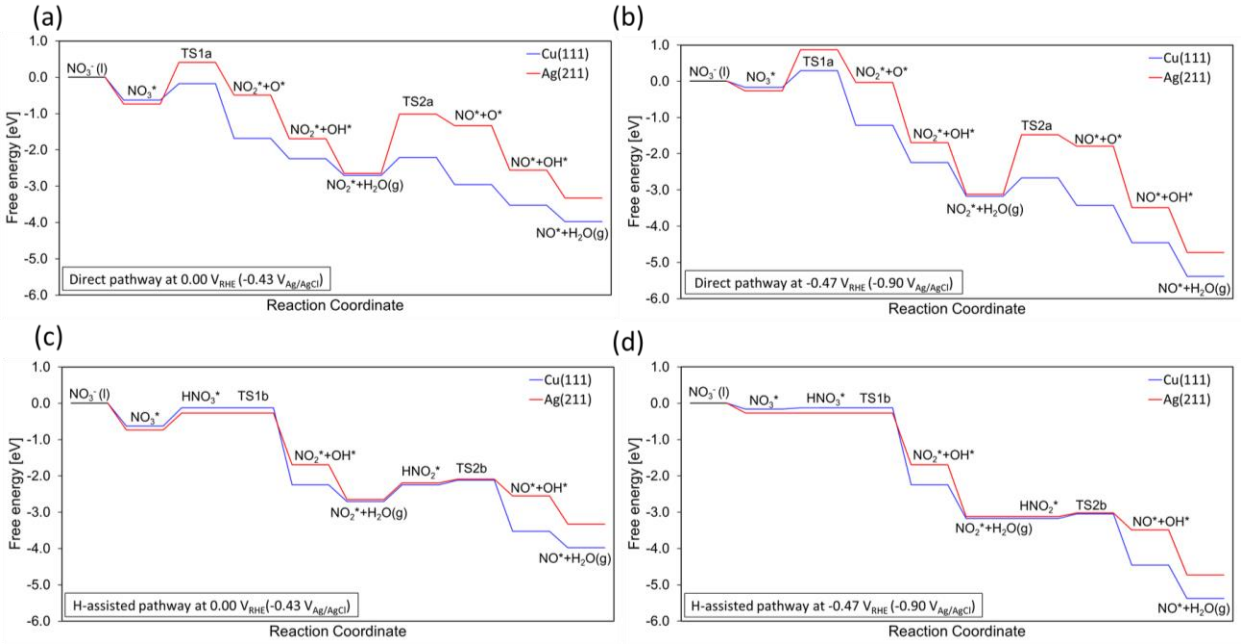

Figure S22. Energy diagrams of the considered reaction pathways of NO_3^- reduction on the two considered surfaces. The direct pathway at (a) 0.00 V_{RHE} and (b) −0.47 V_{RHE} (−0.90 $V_{Ag/AgCl}$). The hydrogen assisted pathway at (c) 0.00 V_{RHE} and (d) −0.47 V_{RHE} (−0.90 $V_{Ag/AgCl}$).

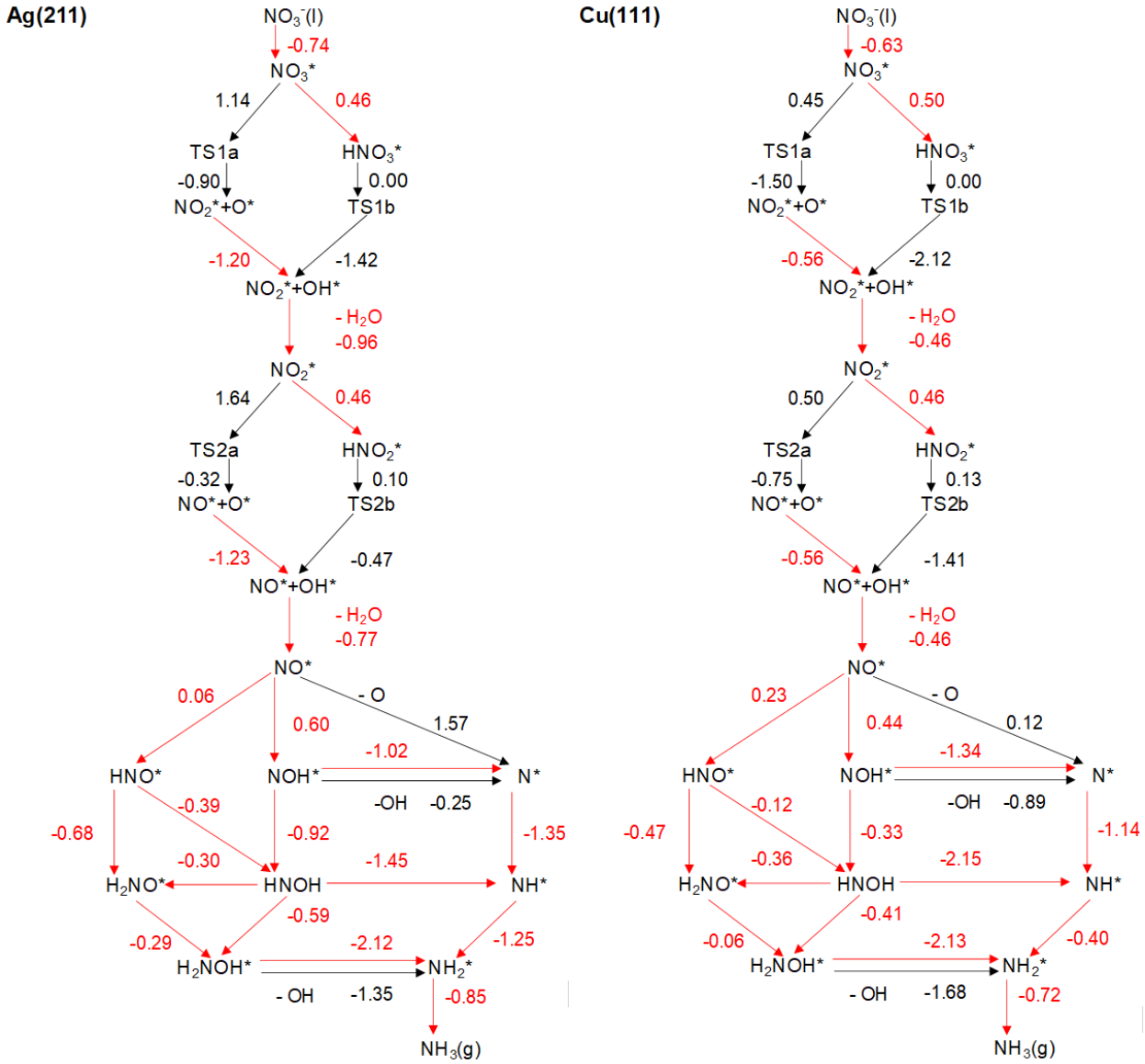

Figure S23. Reaction pathways of reduction of NO_3^-(l) to NH_3(g) on Ag(211) and Cu(111) at 0.00 V_{RHE} (−0.43 $V_{Ag/AgCl}$). All numbers represent the DFT-calculated change in free energy (eV) at the given potential. Red arrows denote electrochemical steps (with proton-electron transfer, potential dependent); black arrows denote non-electrochemical steps (potential independent).

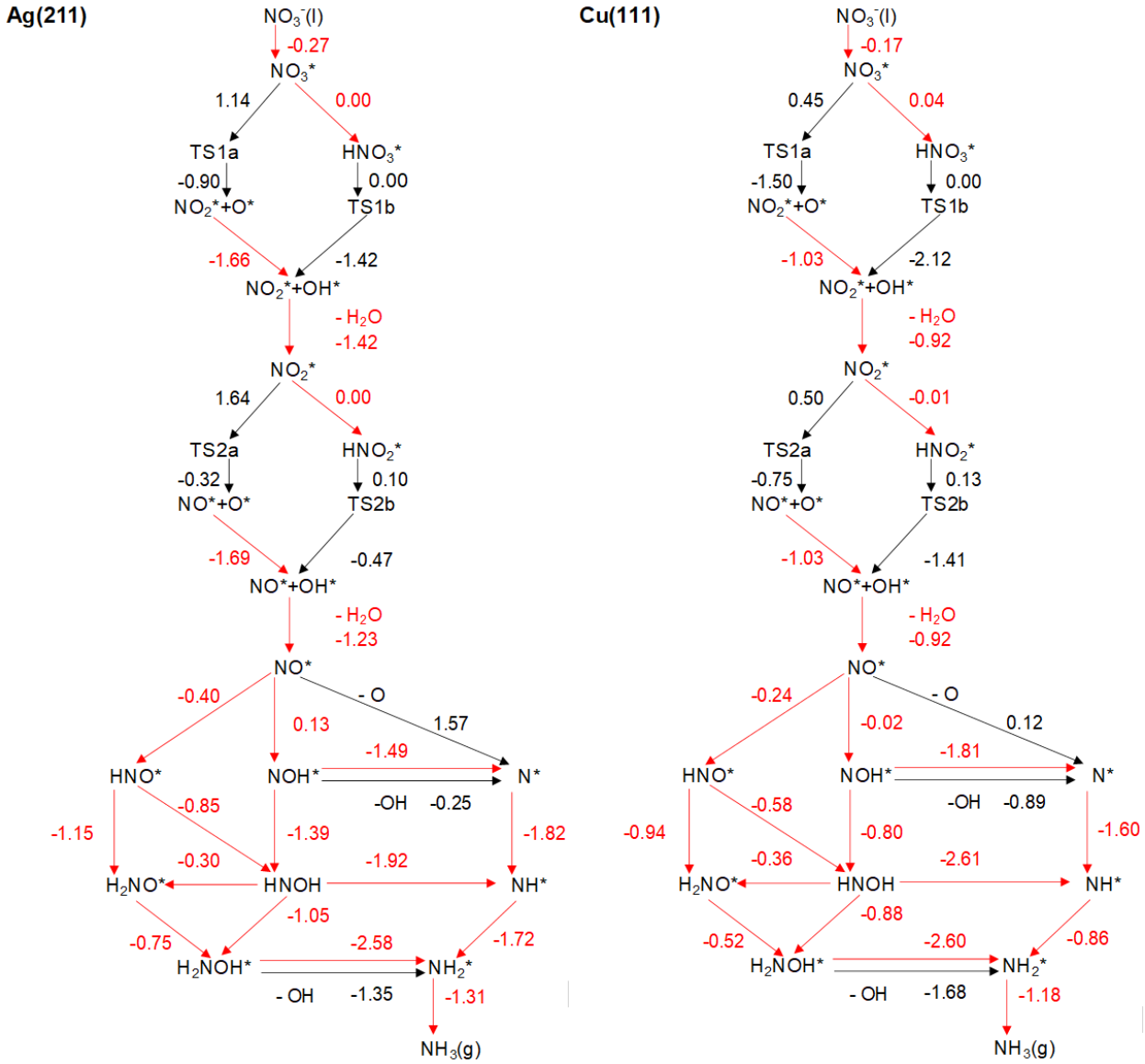

Figure S24. Reaction pathways of reduction of NO_3^-(l) to NH_3(g) on Ag(211) and Cu(111) at −0.47 V_{RHE} (−0.90 $V_{Ag/AgCl}$). All numbers represent the DFT-calculated change in free energy (eV) at the given potential. Red arrows denote electrochemical steps (with proton-electron transfer, potential dependent); black arrows denote non-electrochemical steps (potential independent).

Supplementary Note 2. Potential dependent activation energy of electrochemical steps

As discussed in recent work,[22] the potential dependent activation barrier (E_{act}) for an electrochemical step ($X^* + H^+_{aq} + e^- \rightarrow XH^*$) can be approximated as follows using DFT:

$$U^0 = \frac{-G_{(X+H)^*} + G_{X^*} + \frac{1}{2}G_{H_2(g)}}{e^-}$$

$$E_{act} = E^0_{act}(U^0) + e\beta(U - U^0)$$

where β is the reaction symmetry factor, $E^0_{act}(U^0)$ is the activation energy of the non-electrochemical reduction reaction, and U is the applied potential.

As an example in our work, we applied this to the formation of HNO_3* on Cu(111):

$$U^0 = \frac{-G_{(H+NO_3)^*} + G_{NO_3^*} + \frac{1}{2}G_{H_2(g)}}{e^-} = -0.03 \text{ V vs. RHE}$$

$$e\beta(U - U^0) = e \times 0.5(-0.47 \text{ V} + 0.03 \text{ V}) = -0.22 \text{ eV}$$

We also applied this to the same reaction step on Ag(211):

$$U^0 = \frac{-G_{(H+NO_3)^*} + G_{NO_3^*} + \frac{1}{2}G_{H_2(g)}}{e^-} = -0.38 \text{ eV vs. RHE}$$

$$e\beta(U - U^0) = e \times 0.5(-0.47 \text{ V} + 0.38 \text{ V}) = -0.05 \text{ eV}$$

In the above calculation, β was assumed to be 0.5, as done in previous work.[23] When U was −0.47 V_{RHE}, equivalent to −0.90 $V_{Ag/AgCl}$ at which we present energetics in Figure 4 of the main text, the activation barrier could decrease by 0.21 eV and 0.05 eV on Cu(111) and Ag(211), respectively, due to the applied potential. We do not calculate explicit values of $E^0_{act}(U^0)$ for these reaction steps in this work, though note that previous work has shown, e.g., water-mediated proton transfers to have small barriers of 0.15 eV or less.[22] We also note that a previous DFT study[24] reported the formation of HNO_3 from NO_3 and H is exothermic with no barrier in the gas phase. Although the linearity assumption in this formulation may break down at highly negative potentials (i.e., the calculated reduction in barrier for Cu(111) might actually exceed the barrier itself), we nonetheless anticipate that the substantial reduction in activation energy will render the corresponding steps effectively barrierless (regardless of the actual calculated reduction) at such negative potentials. We therefore on this basis justify our assumption that these barriers are governed essentially by the free energy change of the corresponding reactions at the potentials relevant to this study (−0.90 $V_{Ag/AgCl}$ and more reducing values).

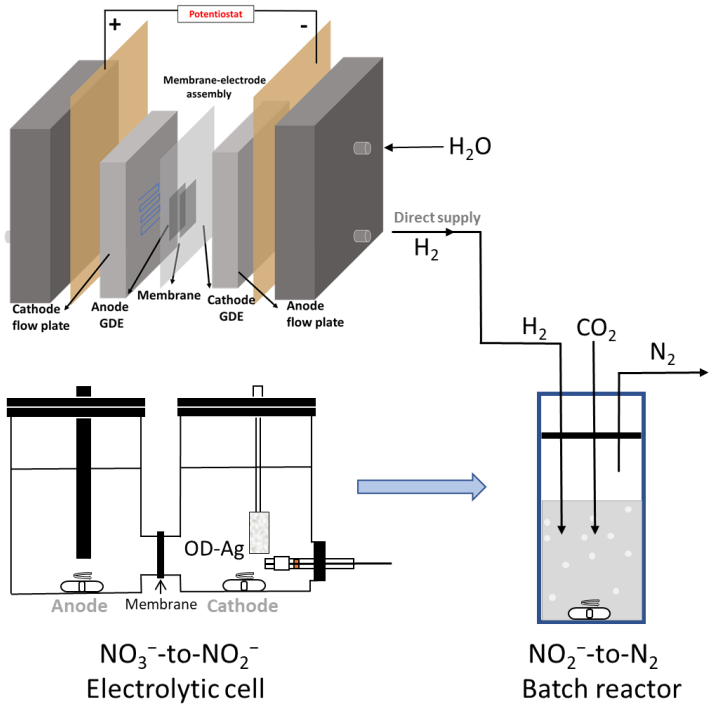

Figure S25. The experimental set-up of the electrocatalytic-catalytic combined process, and H_2 feed was generated from a PEM water electrolyzer.

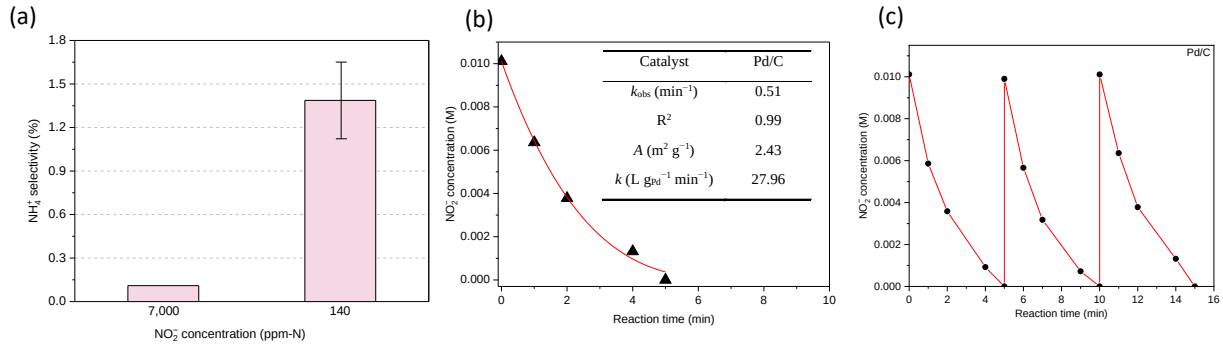

Figure S26. Catalytic reduction of NO_2^- on Pd/C. The reaction medium was 0.1 M KCl with 0.1 M KOH saturated by CO_2. The catalyst loading was 50 mg. (a) Selectivity of NH_4^+ after full conversion of 7,000 and 140 ppm of NO_2^--N. The error bar represents the standard deviation of three independent measurements. (b) NO_2^- concentration profile during its catalytic reduction. The fitted curve assumes pseudo-first-order dependence on NO_2^- concentration. The observed rate constant (k_{obs}), the active surface area of Pd (A), and surface Pd-normalized rate constant (k) are shown in the inset table. (c) NO_2^- concentration profile for three consecutive measurements.

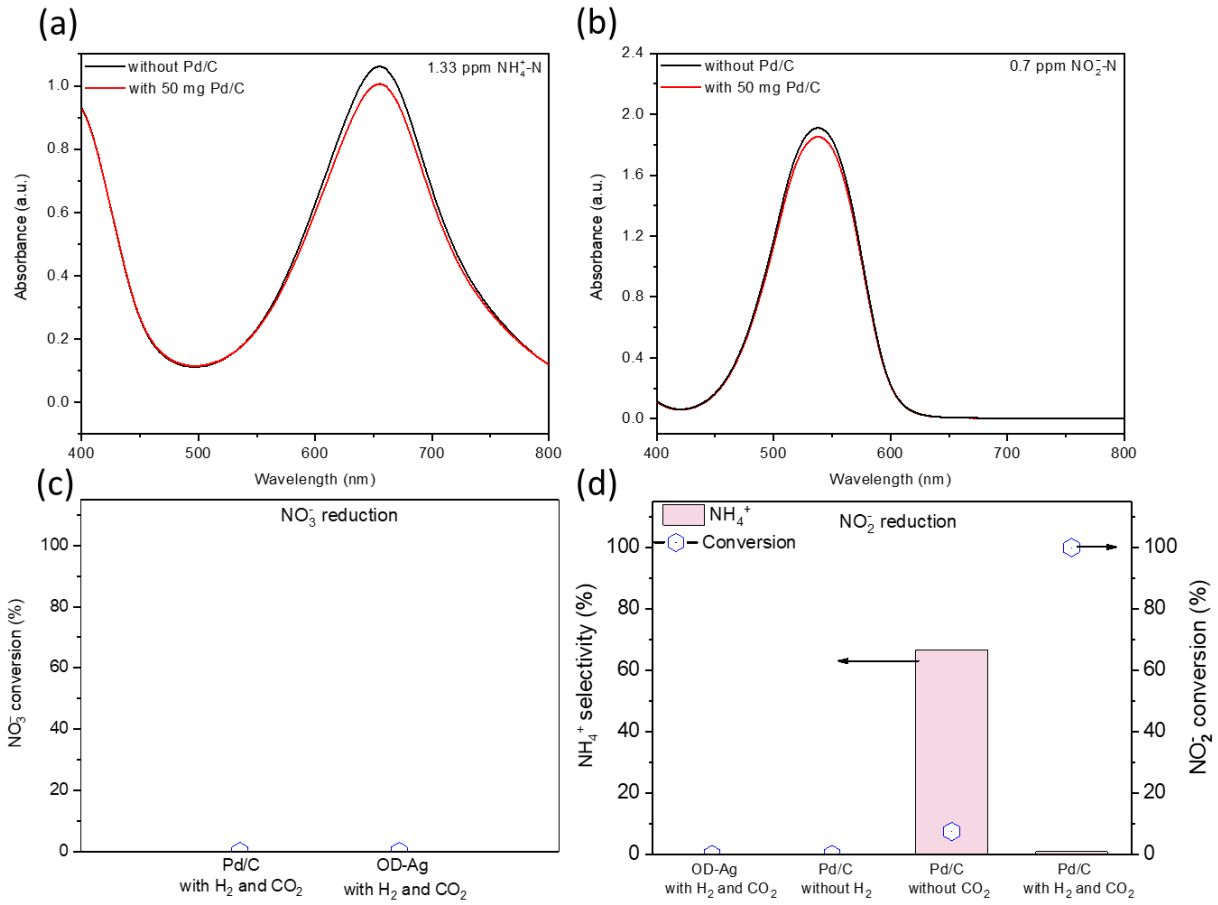

Figure S27. Control experiments for catalytic reduction of NO_3^- and NO_2^-. The conditions for control experiments (a)-(b) were the same as catalytic reduction tests, except that no H_2 was fed. (a) UV-Vis spectra for 1.33 ppm of NH_4^+-N in CO_2-saturated electrolyte stained with indophenol blue indicator, with or without adding 50 mg of Pd/C. (b) UV-Vis spectra for 0.7 ppm of NO_2^--N in CO_2-saturated electrolyte stained with Griess reagent, with or without adding 50 mg of Pd/C. The adsorption of NH_4^+ and NO_2^- contributed to a decrease of 5.2% and 3.0% in the measured concentrations, respectively.

(c) Conversion for catalytic reduction of 0.01 M NO_3^- by H_2 in CO_2-saturated 0.1 M KCl and 0.1 M KOH (15 mL) with 1) 50 mg of 5% Pd/C for 2 h; 2) OD-Ag (4 cm^2 geometric area) for 1 h. The conversion of NO_3^- was very low (<1%) for both cases.

(d) Conversion and NH_4^+ selectivity for catalytic reduction of 0.01 M NO_2^- in CO_2-saturated 0.1 M KCl and 0.1 M KOH (15 mL) with 1) OD-Ag with both H_2 and CO_2 flow for 1 h; 2) 50 mg of 5% Pd/C and no H_2 flow for 1 h; 3) 100 mg of 5% Pd/C and no CO_2 flow for 0.5 h; 4) 50 mg of 5% Pd/C with both H_2 and CO_2 flow for 25 min. The conversion of NO_2^- was negligible (<1%) on OD-Ag and Pd/C without H_2 feed. Without the buffering effect of CO_2, the pH of the electrolyte increased significantly as the reaction proceeded ($2NO_2^- + 3H_2 \rightarrow N_2 + 2OH^- + 2H_2O$). At higher pH, the reaction rate was suppressed, and the production of NH_4^+ became more favorable, which is in accordance with ref.[1]

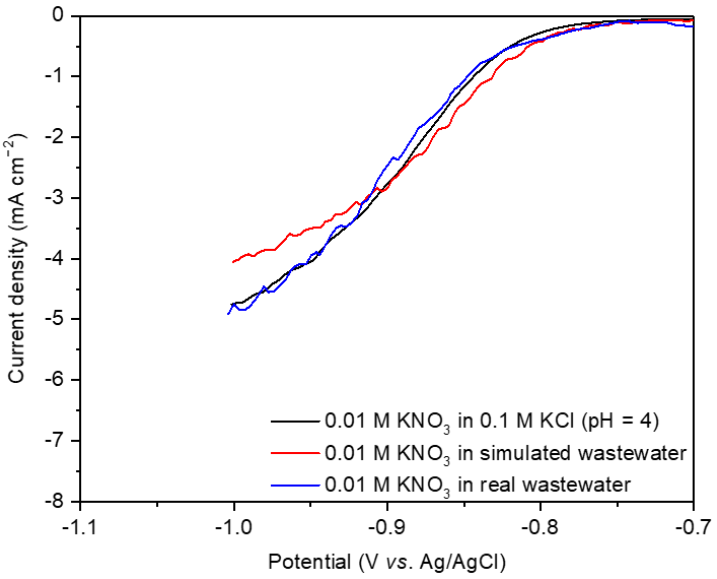

Figure S28. Linear sweep voltammograms of NO3RR in different reaction media. The electrolytes contain 0.01 M NO_3^- (140 ppm-N), and the geometric area of OD-Ag was 6 cm^2.

(a)

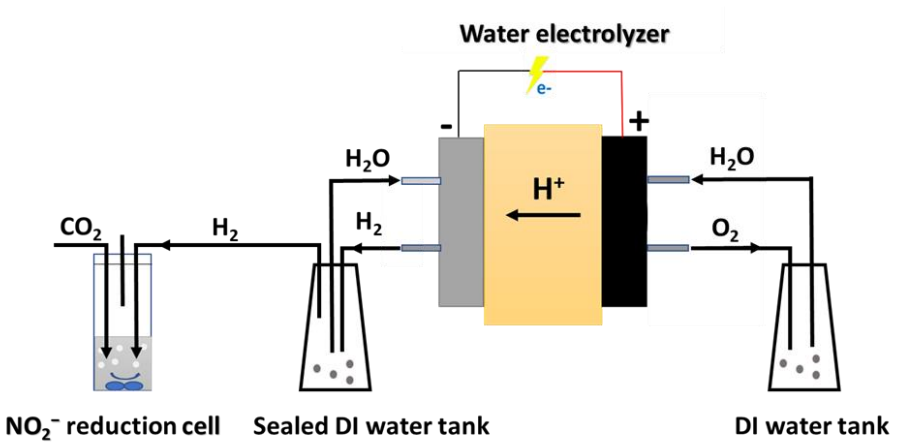

(b)

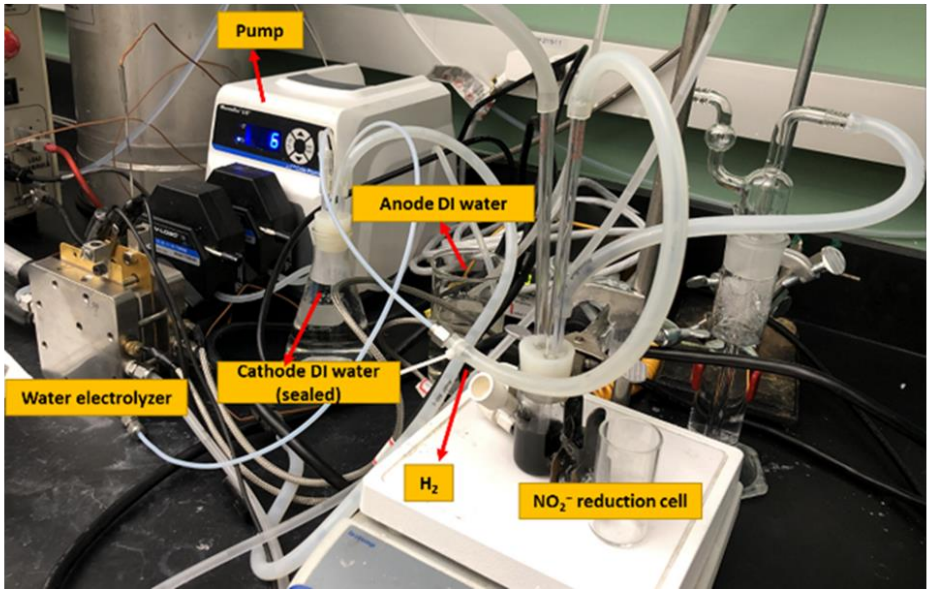

Figure S29. Catalytic reduction of NO_2^- by water-splitting-derived H_2. (a) Schematic illustration and (b) Photograph of the experimental setup. The detailed PEM water electrolyzer set-up was described in the Methods section in the main text. The catalytic reduction conditions were described in the Methods section in the main text, except that H_2 feed was generated from a PEM water electrolyzer. NO_2^- was completely removed within 15 min with 0.9% selectivity to NH_4^+, showing no significant difference with the performance with UHP H_2 feed (**Figure S26**).

Supplementary Note 3. pH effect study for NO3RR on OD-Ag (Figure S30−32).

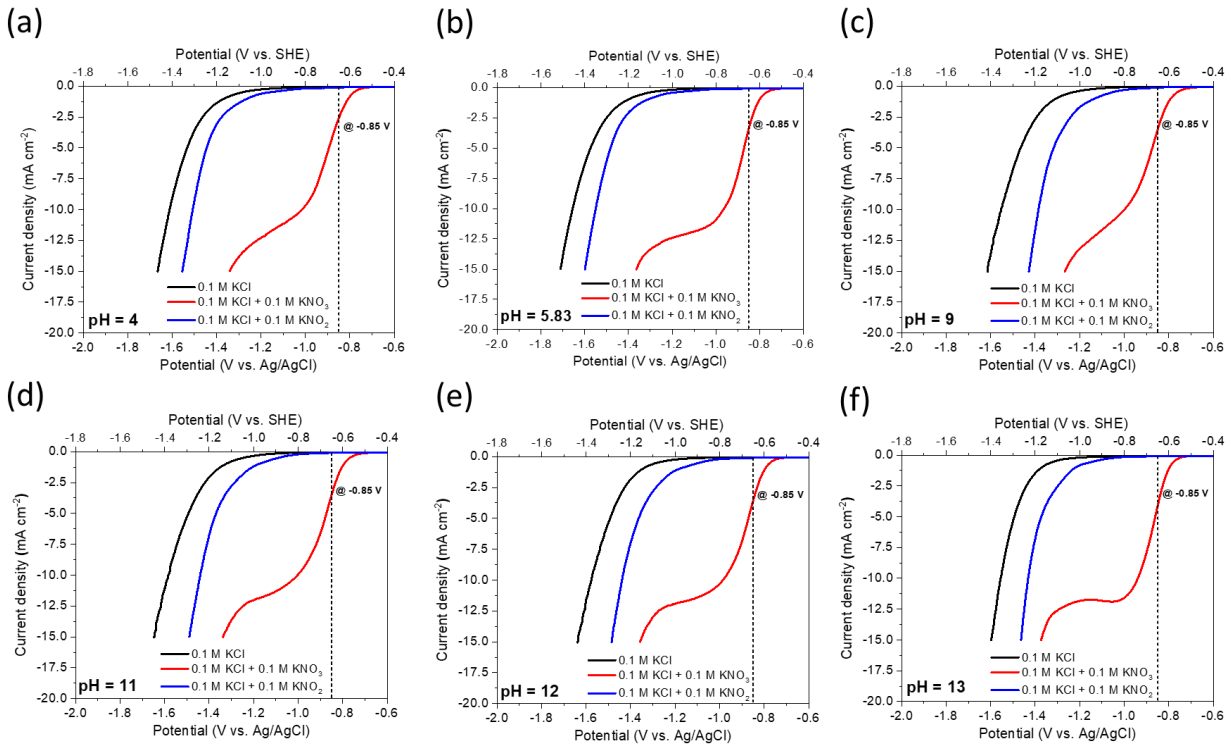

Figure S30. pH effect study for NO3RR on OD-Ag (4 cm^2 geometric area). (a)−(f) Linear sweep voltammetry of OD-Ag in 0.1 M KCl, 0.1 M KCl with 0.1 M NO_3^-, and 0.1 M KCl with 0.1 M NO_2^- at pH 4−13. The current density labeled inside the figures was the data used for the E-pH diagram calculation. The pH of the electrolyte was adjusted by adding HCl or KOH. The SHE scales of potential was calculated by *E* (V *vs.* SHE) = *E* (V *vs.* Ag/AgCl) + 0.197 V.

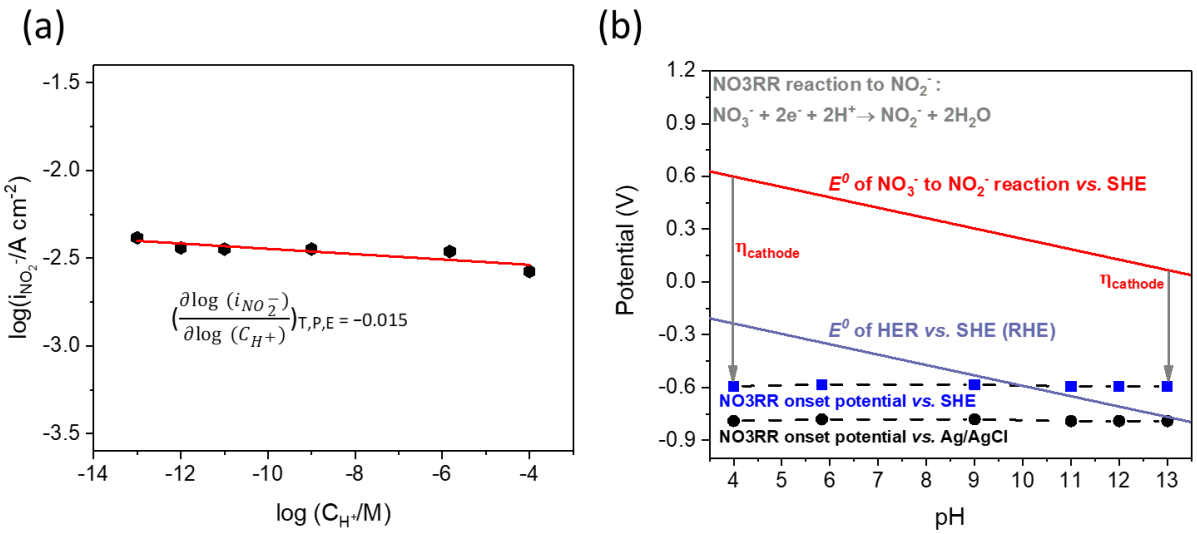

Figure S31. pH effect study for NO3RR on OD-Ag (4 cm^2 geometric area). (a) NO_3^- order dependence fitting in 0.1 M KCl with different concentrations of NO_3^- (pH = 4) at −0.85 $V_{Ag/AgCl}$ with data obtained from LSV curves in **Figure S30**. (b) E-pH diagram for the electroreduction of NO_3^- to NO_2^-.

NO_3^--to-NO_2^- reaction: $NO_3^- + 2H^+ + 2e^- \longrightarrow NO_2^- + 2H_2O$

The observed NO3RR onset potentials in all investigated pH (**Figure S30**) showed similar values versus SHE but different versus RHE. In contrast, the thermodynamic potential E^0 for the reaction of NO_3^--to-NO_2^- is pH-dependent, which is equal to E^0 (NO_3^-/NO_2^-) = 0.835 V – 0.059 × pH. thus, resulting in a lower required overpotential in a higher pH electrolyte. Overpotential ($\eta_{cathode}$) = Onset potential – E^0 (NO_3^-/NO_2^-). The conversion between SHE, RHE, and Ag/AgCl was calculated by: E (V *vs.* SHE) = E (V *vs.* Ag/AgCl) + 0.197 V. E (V *vs.* RHE) = E (V *vs.* Ag/AgCl) + 0.059 × pH + 0.197 V. RHE is pH-dependent, plotted as the thermodynamic potential E^0 for HER: V *vs.* SHE = 0 – 0.059 × pH.

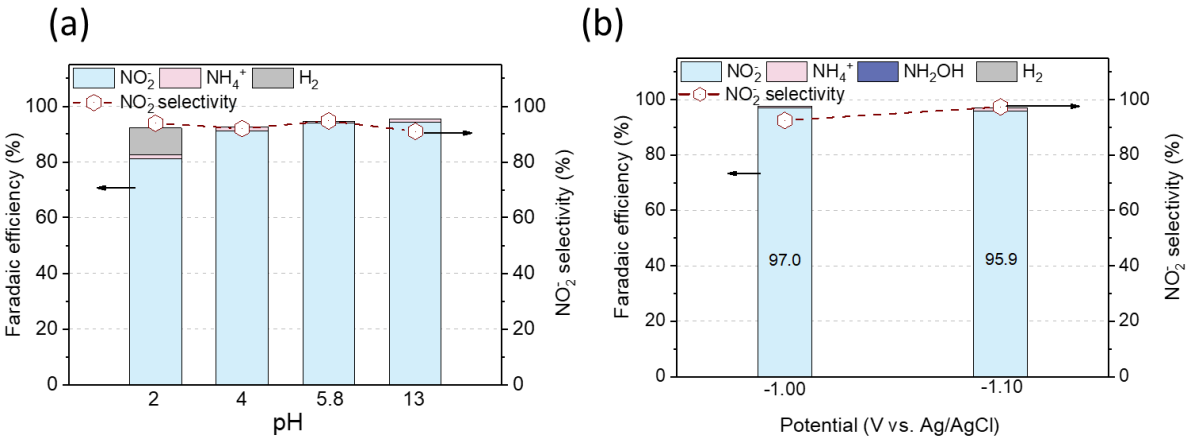

Figure S32. pH effect study for NO3RR on OD-Ag (4 cm^2 geometric area). (a) FE of different products and NO_2^- selectivity at a constant current (25 mA) for 1 h. (b) FE of different products and NO_2^- selectivity at constant voltages (−1.00 V and −1.10 V *vs.* Ag/AgCl) for 1 h at pH 13. The constant current and constant potential tests were performed in 15 mL of 0.1 M KCl with 0.1 M NO_3^- at different pH. The almost identical NO_2^- selectivity and NO_2^- faradaic efficiency at different pH suggested that the potential-controlled selectivity can be maintained in a broad range of pH.

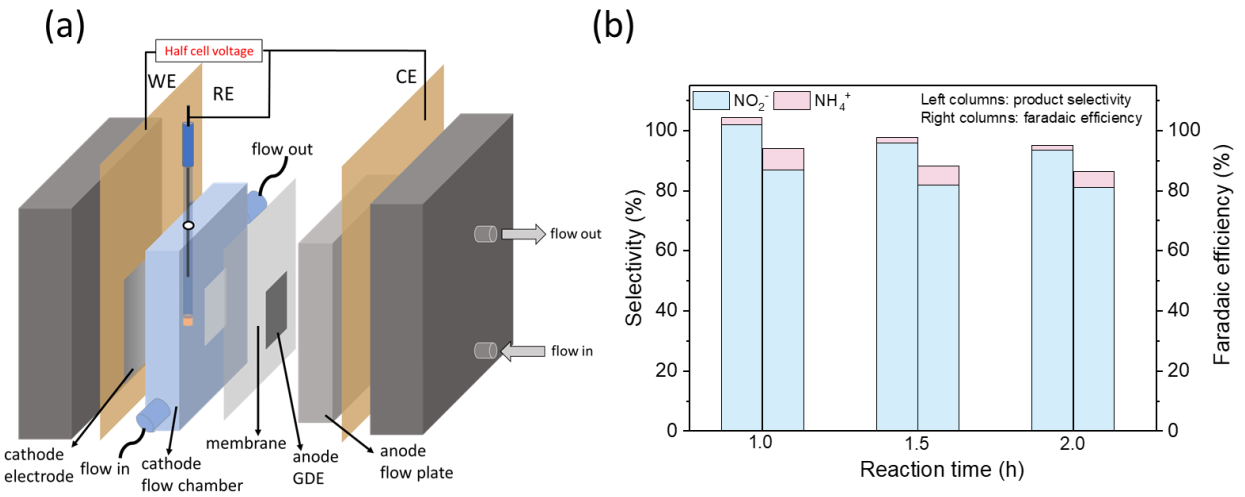

Figure S33. NO3RR in a three-electrode flow cell on OD-Ag (4 cm^2 geometric area). (a) Scheme illustration of the three-electrode flow cell. (b) product selectivity and Faradaic efficiency at constant voltage of −1.15 $V_{Ag/AgCl}$ for different reaction time. The tests were performed in 15 mL of 0.1 M KCl (pH = 4) with 0.1 M NO_3^-. The three-electrode single electrolysis cell contained stainless-steel endplates, gold current collectors, a PTFE flow chamber (cathode) with a hole to insert Ag/AgCl reference, an Nafion membrane (K^+ form), and a flow-field graphite plate (anode). Peristaltic pumps (Masterflex® L/S®) circulated catholyte and anolyte both of 25 ml min^{-1} inside 1/8 silicon tubes (Masterflex).

Supplementary Tables (1–12)

Table S1. Summary of onset potentials ($V_{Ag/AgCl}$, defined as the potential in which the current density attained −0.75 mA cm^{-2}) and onset potential difference on different electrodes. The linear sweep voltammograms are shown in **Figure S1** and **Figure 1b–c.**

Electrode	E_{NO3RR} ($V_{Ag/AgCl}$)	E_{NO2RR} ($V_{Ag/AgCl}$)	E_{HER} ($V_{Ag/AgCl}$)	$E_{NO3RR} - E_{NO2RR}$ (mV)	$E_{NO3RR} - E_{HER}$ (mV)
Ti	−1.37	−1.21	−1.51	−160	140
Pt	−0.91	−0.76	−0.90	−150	−10
Zr	−1.56	−1.41	−1.65	−150	90
Fe	−1.08	−0.94	−1.14	−140	60
Ni	−0.95	−0.81	−1.11	−140	160
Pd	−1.07	−1.00	−1.10	−70	30
Au	−1.26	−1.21	−1.33	−50	70
V	−1.30	−1.25	−1.40	−50	100
Mo	−1.23	−1.19	−1.21	−40	−20
Bi	−1.42	−1.38	−1.52	−40	100
Co	−0.84	−0.80	−1.21	−40	370
Zn	−1.33	−1.30	−1.61	−30	280
Sn	−1.68	−1.66	−1.64	−20	−40
Al	−1.98	−1.96	−1.91	−20	−70
W	−1.24	−1.23	−1.27	−10	30
Pb	−1.60	−1.60	−1.71	0	110
Cu	−0.94	−0.99	−1.35	50	410
Ag	−1.00	−1.41	−1.53	410	530

Table S2. Summary of state-of-the-art NO3RR electrocatalysts for NH_3 production. "N/A" indicates the parameter is not available in the publication.

NO_3^- concentration (ppm-N)	Catalyst	NO_3^- conversion (%)	FE of NH_3 (%)	Ref.
500	O-Cu–PTCDA	N/A	85.9	[25]
200	Cu/Cu_2O NWAs	97	95.8	[26]
140	$Cu_{50}Ni_{50}$ alloy	N/A	93	[27]
3000	Porous Cu	73	72	[28]
140	Cu nanosheets	N/A	99.7	[29]
280	Co-NAs	N/A	96	[30]
200	Co/CoO NSAs	80.8	93.8	[31]
100	Pd/Cu_2O	99.8	94.3	[32]
1400	Ti	N/A	82	[33]
50	TiO_{2-x}	95.2	85.0	[34]
14000	Ir NTs	N/A	84.7	[35]
14000	Ru-ST	N/A	96	[36]
140	OD-Ag	99	89	**This work**

Table S3. Content of gaseous products (NO_2, NO, and N_2O) for the electro-reduction of NO_3^- or NO_2^- on OD-Ag. The electrolyte was 0.1 M KCl and the applied potential was −1.50 $V_{Ag/AgCl}$.

Entry	Reactants	Ar flow rate (mL min^{-1})	Reaction time (min)	Product detected	Content (ppm)	Charge (C)
1	0.05 M NO_3^-	12.5	4	Total NO + NO_2	3.0	25.4
2	0.025 M NO_3^- + 0.025 M NO_2^-	20	35	N_2O	32.6	190.7
3	0.025 M NO_3^- + 0.025 M NO_2^-	12.5	4	Total NO + NO_2	2.4	21.2

Note: Estimation of FE of N_2O based on Entry 2

$$n_{N_2O} = 20\ \text{mL}\ \text{min}^{-1} \times 35\ \text{min} \times 32.6\ \times 10^{-6} \times 0.0416\ \text{mol}\ \text{L}^{-1}/1000 = 9.49 \times 10^{-7}\ (\text{mol})$$

Assuming all N_2O was reduced from NO_3^- (NO_2^-), the upper (lower) limit of FE is

$$FE_{N_2O,max} = \frac{9.49 \times 10^{-7}\ \text{mol} \times 4 \times 96485\ \text{C}\ \text{mol}^{-1}}{190.7\ \text{C}} \times 100\% = 0.19\%$$

$$FE_{N_2O,min} = \frac{9.49 \times 10^{-7}\ \text{mol} \times 2 \times 96485\ \text{C}\ \text{mol}^{-1}}{190.7\ \text{C}} \times 100\% = 0.096\%$$

Similarly, results in the above table show a negligible contribution of NO_2 and NO (≤0.007%) to the total FE in the system.

Table S4. Calculated zero-point energy corrections, entropies, and free energies of adsorbed species on Ag(111), and Pd(111) with respect to NO_3^-(l), H_2(g), and H_2O(g) at 0.00 V_{RHE}.

	ZPE [eV]	*S* [J/mol-K]	$\Delta G_{Ag(111)}$ [eV]	$\Delta G_{Pd(111)}$ [eV]
H*	0.17	1.79	0.40	-0.40
O*	0.07	12.26	2.20	1.28
OH*	0.33	29.41	0.94	1.03
NO_3*	0.40	88.43	−0.37	−0.30
HNO_3*	0.69	91.61	−0.17	−0.18
NO_2*	0.27	67.54	−2.35	−2.49
HNO_2*	0.56	91.76	−2.13	−2.21
NO*	0.14	60.01	−3.26	−5.18
HNO*	0.40	48.19	−3.09	−4.33
NOH*	0.49	33.00	−0.59	−4.21
HNOH*	0.82	48.52	−1.15	−4.27
H_2NO*	0.82	46.55	−1.56	−4.27
H_2NOH*	1.11	80.00	−2.15	−4.64
N*	0.09	8.15	−3.33	−5.98
NH*	0.39	11.90	−4.88	−6.43
NH_2*	0.69	24.21	−5.89	−6.55
NH_3*	1.01	40.56	−6.72	−7.15

Table S5. Calculated zero-point energy corrections, entropies, and free energies of Ag(211) with respect to NO_3^-(l), H_2(g), and H_2O(g) at 0.00 V_{RHE}.

	ZPE [eV]	*S* [J/mol-K]	$\Delta G_{Ag(211)}$
H*	0.15	2.82	0.46
O*	0.05	20.90	1.99
OH*	0.34	36.63	0.77
NO_3*	0.39	102.03	−0.74
HNO_3*	0.68	74.42	−0.27
NO_2*	0.26	84.53	−2.65
HNO_2*	0.52	67.39	−2.19
NO*	0.15	43.64	−3.32
HNO*	0.42	47.50	−3.26
NOH*	0.42	66.07	−2.73
HNOH*	0.76	63.68	−3.65
H_2NO*	0.80	69.46	−3.95
H_2NOH*	1.10	66.63	−4.23
N*	0.06	18.80	−3.75
NH*	0.35	20.65	−5.10
NH_2*	0.68	33.12	−6.35
NH_3*	0.98	51.10	−6.89

Table S6. Calculated zero-point energy corrections, entropies, and free energies of Cu(111) with respect to NO_3^-(l), H_2(g), and H_2O(g) at 0.00 V_{RHE}. Bolded numbers are Cu(111)-based *ZPE* and *S*; other values are taken from Pd(111).

	ZPE [eV]	*S* [J/mol-K]	$\Delta G_{Cu(111)}$
H*	0.17	1.79	0.01
O*	**0.07**	**12.37**	**1.02**
OH*	**0.34**	**25.55**	**0.46**
NO_3*	**0.40**	**74.93**	**−0.63**
HNO_3*	**0.69**	**75.79**	**−0.13**
NO_2*	**0.27**	**70.04**	**−2.70**
HNO_2*	**0.55**	**75.19**	**−2.25**
NO*	**0.16**	**44.03**	**−3.98**
HNO*	0.40	48.19	−2.31
NOH*	0.49	33.00	0.19
HNOH*	0.82	48.52	−0.36
H_2NO*	0.82	46.55	−0.78
H_2NOH*	1.11	80.00	−1.36
N*	0.09	8.15	−2.55
NH*	0.39	11.90	−4.10
NH_2*	0.69	24.21	−5.11
NH_3*	1.01	40.56	−5.94

Table S7. Calculated activation energies (enthalpies) [eV] of direct and H-assisted pathways on the surfaces considered in this study.

	NO_3* dissociation		NO_2* dissociation	
	Direct	H-assisted	Direct	H-assisted
Ag(211)	1.14	0.12	1.68	0.18
Cu(111)	0.51	0.06	0.55	0.15
Ag(111)	1.12	0.13	–	–
Pd(111)	0.57	0.14	–	–

Table S8. The most stable adsorption configurations of NO_3*, HNO_3*, and NO_2* (top view). Atom colors for adsorbed species: N (light blue), O (red), H (white). The unit cell is shown with black lines.

	NO_3*	HNO_3*	NO_2*
Ag(111)	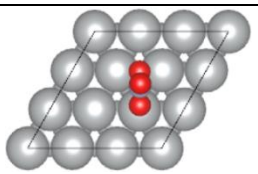	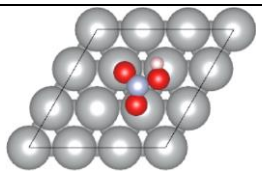	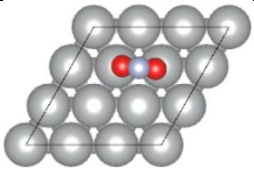
Pd(111)	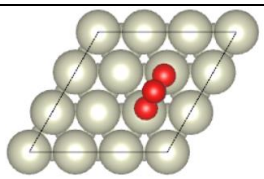	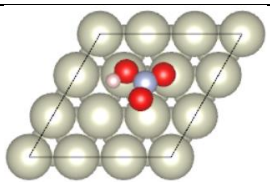	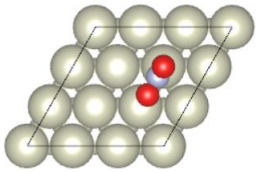

Table S9. Content of NO and N_2O products for the catalytic reduction of 0.5 M NO_2^-. Reaction conditions and calculation of flow rate are detailed in the **Experimental Section**.

Reaction time (min)	Converted NO_2^- (mol)	Detected NO (ppm)	Detected N_2O (ppm)
10	0.0075 (for *t* = 0–120 min)	7.2	165.2 (for *t* = 0–60 min)
15		3.6	
20		2.4	
40		1.0	
60		<1.0[a]	
80		<1.0	236.3 (for *t* = 60–120 min)
100		<1.0	
120		<1.0	

[a] "<1.0 ppm" indicates the NO content was below the detection limit (1.0 ppm) of the nitrogen oxides detector tube.

Note: Estimation of selectivity to NO and N_2O for *t* = 0–120 min

$$n_{N_2O} = 14\ \text{mL}\ \text{min}^{-1} \times 60\ \text{min} \times (165.2 + 236.3) \times 10^{-6} \times 0.0415\ \text{mol}\ \text{L}^{-1}/1000$$
$$= 1.40 \times 10^{-5}\ (\text{mol})$$

The selectivity of N_2O is

$$S_{N_2O} = \frac{1.40 \times 10^{-5}\ \text{mol}}{0.0075\ \text{mol}} \times 100\% = 0.19\%$$

Similarly, the estimated selectivity to NO is 0.0009% for *t* = 0–120 min.

Table S10. Summary of the experimental results of the combined denitrification process.

		Step 1 (Electro-reduction on OD-Ag)					Step 2 (Catalytic reduction on Pd/C)			
Reaction medium	c_0 (NO_3^-) (ppm-N)	Potential (V)[a]	Charge (C)	FE (NO_2^-)	FE (H_2)	X (NO_3^-)[b]	S (NH_4^+)[c]	c (NO_3^-) (ppm-N)	c (NO_2^-) (ppm-N)	c (NH_4^+) (ppm-N)
0.1 M KCl (pH = 4)	140	−1.10	31.5	82.0%	4.9%	98.8%	1.8%	1.7	–[d]	2.4
	140	−1.00	31.5	82.0%	2.1%	95.9%	1.3%	5.9	–	1.8
	140	−1.00	31.5	85.2%	2.7%	93.1%	1.6%	9.7	–	2.1
	140	−1.00	31.5	84.1%	1.9%	96.1%	1.8%	5.7	–	1.7
	140	−1.00	29.5	84.6%	2.3%	90.9%	1.5%	12.6	–	1.8
	70	−1.00	14.5	84.0%	1.6%	92.9%	1.3%	5.0	–	0.8
Simulated[e]	140	−1.00	33.5	80.6%	3.8%	97.4%	1.6%	1.7	–	2.4
Real[f]	140	−1.00	35.3	78.5%	3.2%	98.4%	2.5%	3.6	–	3.5

[a] Potential (V) *vs.* Ag/AgCl.

[b] Conversion of NO_3^-.

[c] Selectivity to NH_4^+.

[d] "–" indicates the level of NO_2^- was below the detection limit of 1 μM of the colorimetric method.

[e] Simulated waste stream from the ion-exchange columns.[37]

[f] Real agricultural wastewater from Des Moines Water Works, Iowa.

Table S11. Summary of the reported electrocatalytic or catalytic systems for NO_3^- removal. "N/A" indicates the parameter is not available in the publication.

c_0 (NO_3^-) (ppm-N)	System	Catalyst	X (NO_3^-)[a]	S (N_2)[b]	S (NO_x)[c]	S (gases)[d]	S (NH_4^+)[e]	Ref.
700	Electrocatalytic	Cu	90%	1%	0.1%	N/A	77.3	[38]
112	Electrocatalytic	Blended $Sn_{0.8}Pd_{0.2}$/S	100%	81%	0	N/A	14[f]	[39]
700	Electrocatalytic	Sn	99%	92%	0	N/A	8%	[20]
700	Electrocatalytic	Bi	95%	65%	16%	N/A	19%	[40]
50	Electrocatalytic	nZVI@OMC	65%	N/A	N/A	74%	26%	[41]
140	Electrocatalytic	BDD	48%	45%	0	N/A	7%[g]	[42]
140	Electrocatalytic	Sn/PdPt	59%	44%	25%	N/A	13%	[43]
50	Electrocatalytic	$Pd_{0.27}Cu_{0.73}$/SS	99%	65%	0.3%	N/A	34%	[44]
700	Electrocatalytic	$Bi_{60}Sn_{40}$/C/TP	N/A	50%	0	N/A	40%	[45]
135	Electrocatalytic	Pd/Al_2O_3 on Cu	59%	35%	N/A	N/A	35%	[46]
50	Electrocatalytic	Cu/Ni	97%	33%	N/A	N/A	67%	[47]
112	Electrocatalytic	SS/$Sn_{0.2}Pd_{0.8}$-497	88%	89%	N/A	N/A	9%	[48]
50	Electrocatalytic	Sn/Ni modified with BZT	99%	66%	N/A	N/A	20%	[49]
100	Electrocatalytic[h]	nZVI@D201	80%	N/A	N/A	95%	N/A	[50]
50	Catalytic	PdIn	100%	N/A	N/A	95%	5%	[51]
100	Catalytic	PdIn	82%	N/A	N/A	74%	26%	[52]
360	Catalytic	PdCu	>90%	N/A	<1%	94%	3%	[53]
30	Catalytic	PdSn	100%	N/A	N/A	91%	9%	[54]
400	Catalytic	Ni/Al_2O_3	79%	N/A	N/A	53%	38%	[55]
100	Catalytic	Pd-Cu/resin	95%	N/A	N/A	93%	7%	[56]
30	Catalytic	PdCu	99%	N/A	N/A	70%	20%	[57]
140	Electrocatalytic-Catalytic	OD-Ag and Pd/C	98%	93%[i]	N/A	99%	1%	**This work**

[a] Conversion of NO_3^-.

[b] Selectivity to N_2, as calculated by (Reacted NO_3^- − Produced NH_4^+ − Produced NO_2^-) / (Reacted NO_3^-).

[c] Selectivity to NO_x.

[d] Selectivity to gases product, as calculated by (Reacted NO_3^- − Produced NH_4^+ − Produced NO_2^-) / (Reacted NO_3^-).

[e] Selectivity to NH_4^+.

[f] Yield of NH_4^+, as calculated by Conversion of NO_3^- × Selectivity of NH_4^+.

[g] FE of NH_4^+.

[h] Electro-reduction of NO_3^- to NH_4^+ coupled with electro-oxidation of NH_4^+ to N_2.

[i] Selectivity to N_2, as quantified by on-line gas chromatography.

Supplementary Note 4. Technoeconomic Analysis (TEA) Estimation

Assuming the concentration of NO_3^- in wastewater is **40 mg L^{-1}-N**, for the treatment of 1 m^3 of wastewater:

(1) Electrochemical NO_3^--to-NO_2^- step:
$NO_3^- + 2e^- + 2H^+ \rightarrow NO_2^- + H_2O$
Mole of NO_3^--N for 1 m^3 wastewater = (40 mg L^{-1}-N / m^3) / 14 g mol^{-1} = 2.86 mole/m^3

(a) Energy cost
Assuming 2.5 V cell voltage, 85% faradaic efficiency from NO_3^- to NO_2^-, and the renewable electricity price is \$0.02 kWh^{-1}(wind source in the next decade),[58] then:
Electricity consumption = 2.86 (moles) × 96485 (C $mole^{-1}$) × 2 × 2.5 V / 0.85 = 1.623 MJ = 0.45 kWh/m^3
Electricity cost = 0.45 (kWh/m^3) × 0.02 (\$ kWh^{-1}) = \$ **0.009**/m^3

(b) Catalyst cost
Assuming the used Ag is thin and with a lifetime of 1 year; the price of Ag is from BASF catalysts-Metal Prices; and the NO_3^--to-NO_2^- step rate is 5 gallon per minute (equivalent to approximately 2.6 million gallons per year), then:
Catalyst cost = \$ **0.002**/m^3

(2) Catalytic NO_2^--to-N_2 step:
$2NO_2^- + 3H_2 + 2CO_2 \rightarrow N_2 + 2HCO_3^- + 2H_2O$

(a) Chemical cost
Assuming H_2 utilization is 75%, the mole of H_2 needed for treatment of 1 m^3 wastewater = 5.72 mole/m^3
DOE has set the cost target of H_2 production by water electrolysis is 2 \$/kg-H_2.[59] We assume that CO_2 is from industrial waste of ethanol fermentation (~100% purity) with no cost.[60]
Chemical cost = 5.72 (mole/m^3) × 2 (g $mole^{-1}$)/1000 × 2 (\$ kg^{-1}) = \$ 0.023/m^3

(b) Catalyst cost
To have a fair comparison with the previous catalytic approach, we calculated and updated the "Pd-normalized constant" to 3.06 L g_{Pd}^{-1} min^{-1} (based on 0.51 min^{-1} of measured pseudo first-order rate constant, and 50 mg of 5wt.% Pd/C in 15 mL of solution), instead of previous reported "surface Pd-normalized constant" with k = 27.96 L g_{Pd}^{-1} min^{-1} (Figure S26).

We assume 99% of removal rate, and factor (f) will be $-1/\ln(1 - 0.99) = 1/(4.605) = 0.217$. Then, the needed amount of Pd to treat the capacity of 5 gallon-wastewater/min (i.e., Q = 18.92 L/min) will be $Q/(k \cdot f)$ = (18.92 L/min)/[(3.06 L $g_{Pd}^{-1}min^{-1}$) × (0.217)] = 28.49 g-Pd.

We adopted the 5-year-average (2016-2020) cost of Pd metal (from www.Statista.com): \$1,239/oz-Pd = \$39.8/g-Pd. Further, we consider there is 40% of production/manufacturing cost on top of material cost (consistent with BASF Pd catalyst), leading to the cost of Pd catalyst to be \$55.7/g-Pd-catalyst.

We assume the catalyst can work for 5 years. Then, the cost of the Pd catalyst per m^3 of wastewater will be (\$55.7/g-Pd-catalyst)*(28.49 g-Pd-catalyst) × (1000 L/m^3)/[(5 years) × (365 days/year) × (24 hrs/day) × (60 min/hr) × (18.92 L/min)] = \$0.032/m^3.

Total cost of our approach: **\$0.066/m^3** (i.e., 0.009 + 0.002 + 0.023 + 0.032).

Table S12. Summary of the reported cost for wastewater treatment of nitrate.[a]

Methods	Capital Cost ($ m^{-3})	Total Cost ($ m^{-3})
Ion exchange	0.074–0.16	0.17–0.38
Reverse osmosis	0.26–0.34	0.67–0.85
Electrodialysis	0.37	0.55
Biological denitrification	0.16–0.21	0.27–0.30
Catalytic denitrification	0.156[b]	N/A
Our work	**0.066**	N/A

[a] From the ref. 61 in Tables 3.5, 3.7, 3.9, and 3.13 for ion exchange, reverse osmosis, electrodialysis, and biological denitrification methods, respectively, and changed the unit from $ per 1,000 gallons to $ per cubic meter.
[b] The reported data was calculated based the ref. **51** (using H_2 to directly reduce NO_3^- to N_2), with one of the best performances (highest selectivity of 95%) in this filed.

Estimation of capital cost for the catalytic denitrification approach (ref. 51):

$2NO_3^- + 5H_2 + 2CO_2 \rightarrow N_2 + 2HCO_3^- + 4H_2O$

(1) Chemical cost
Assuming the H_2 utilization is the same as 75%, the mole of H_2 needed for treatment of 1 m^3 wastewater = 9.53 mole/m^3
Further assuming the cost of H_2 production is the same as 2 $/kg-$H_2$;[59] and the cost of CO_2 is free as well.[60]
Chemical cost = 9.53 (mole) × 2 (g $mole^{-1}$) × 2 ($ kg^{-1}) = $ 0.038/m^3

(2) Catalyst cost
The catalyst in that paper is In-Pd (40sc%, with 5wt%:95wt.% of In:Pd), and the rate constant of pseudo first-order reaction is 0.087 min^{-1} (0.553 mg-In and 10.507 mg-Pd in 99.5 mL of solution). The "Pd-normalized constant" is 0.823 L g_{Pd}^{-1} min^{-1}.

We ignored the cost of In because of its low composition and low cost, as compared with Pd, $218/oz-In *vs.* $1,239/oz-Pd (based on the 5-year-average cost from the same website).

Similarly, the calculated catalyst cost is $0.118/$m^3$.

Total cost: **$0.156/$m^3$** (i.e., $0.118 + $0.038)

References

(1) Martínez, J.; Ortiz, A.; Ortiz, I., State-of-the-art and perspectives of the catalytic and electrocatalytic reduction of aqueous nitrates. *Appl. Catal. B* **2017,** *207*, 42–59.
(2) Clark, C. A.; Reddy, C. P.; Xu, H.; Heck, K. N.; Luo, G.; Senftle, T. P.; Wong, M. S., Mechanistic Insights into pH-Controlled Nitrite Reduction to Ammonia and Hydrazine over Rhodium. *ACS Catal.* **2019,** *10* (1), 494–509.
(3) Paidar, M.; Roušar, I.; Bouzek, K., Electrochemical removal of nitrate ions in waste solutions after regeneration of ion exchange columns. *J. Appl. Electrochem.* **1999,** *29* (5), 611–617.
(4) Kresse, G.; Furthmüller, J., Efficient iterative schemes for ab initio total-energy calculations using a plane-wave basis set. *Phys. Rev. B* **1996,** *54* (16), 11169–11186.
(5) Kresse, G.; Furthmüller, J., Efficiency of ab-initio total energy calculations for metals and semiconductors using a plane-wave basis set. *Comput. Mater. Sci.* **1996,** *6* (1), 15–50.
(6) Blöchl, P. E., Projector augmented-wave method. *Phys. Rev. B* **1994,** *50* (24), 17953–17979.
(7) Kresse, G.; Joubert, D., From ultrasoft pseudopotentials to the projector augmented-wave method. *Phys. Rev. B* **1999,** *59* (3), 1758–1775.
(8) Perdew, J. P.; Wang, Y., Accurate and simple analytic representation of the electron-gas correlation energy. *Phys. Rev. B* **1992,** *45* (23), 13244–13249.
(9) William M Haynes; David R Lide; Thomas J Bruno. CRC Handbook of Chemistry and Physics (Ed.:W.M.Haynes). CRC (2016).
(10) Monkhorst, H. J.; Pack, J. D., Special points for Brillouin-zone integrations. *Phys. Rev. B* **1976,** *13* (12), 5188–5192.
(11) Calle-Vallejo, F.; Huang, M.; Henry, J. B.; Koper, M. T.; Bandarenka, A. S., Theoretical design and experimental implementation of Ag/Au electrodes for the electrochemical reduction of nitrate. *Phys. Chem. Chem. Phys.* **2013,** *15* (9), 3196–3202.
(12) Krukau, A. V.; Vydrov, O. A.; Izmaylov, A. F.; Scuseria, G. E., Influence of the exchange screening parameter on the performance of screened hybrid functionals. *J. Chem. Phys.* **2006,** *125* (22), 224106.
(13) Nørskov, J. K.; Rossmeisl, J.; Logadottir, A.; Lindqvist, L.; Kitchin, J. R.; Bligaard, T.; Jónsson, H., Origin of the Overpotential for Oxygen Reduction at a Fuel-Cell Cathode. *J. Phys. Chem. B* **2004,** *108* (46), 17886–17892.
(14) Chou, S.-S.; Chung, J.; Hwang, D., A high performance liquid chromatography method for determining nitrate and nitrite levels in vegetables. *J. Food Drug Anal.* **2003,** *11* (3), 233–238.
(15) Chen, Y.; Liu, H.; Ha, N.; Licht, S.; Gu, S.; Li, W., Revealing nitrogen-containing species in commercial catalysts used for ammonia electrosynthesis. *Nature Catal.* **2020**, 1–7.
(16) Kim, K.; Chen, Y.; Han, J.-I.; Yoon, H. C.; Li, W., Lithium-mediated ammonia synthesis from water and nitrogen: a membrane-free approach enabled by an immiscible aqueous/organic hybrid electrolyte system. *Green Chem.* **2019,** *21* (14), 3839–3845.
(17) Burrell, D. S. F. a. R. C., Spectrophotometric Method for Determining Hydroxylamine Reductase Activity in Higher Plants. *Anal. Chem.* **1955,** *27*, 1664–1665.
(18) Kim, C.; Jeon, H. S.; Eom, T.; Jee, M. S.; Kim, H.; Friend, C. M.; Min, B. K.; Hwang, Y. J., Achieving Selective and Efficient Electrocatalytic Activity for CO_2 Reduction Using Immobilized Silver Nanoparticles. *J. Am. Chem. Soc.* **2015,** *137* (43), 13844–13850.
(19) Prelazzi, G.; Cerboni, M.; Leofanti, G., Comparison of H_2 Adsorption, O_2 Adsorption, H_2 Titration, and O_2 Titration on Supported Palladium Catalysts. *J. Catal.* **1999,** *181* (1), 73–79.
(20) Katsounaros, I.; Ipsakis, D.; Polatides, C.; Kyriacou, G., Efficient electrochemical reduction of nitrate to nitrogen on tin cathode at very high cathodic potentials. *Electrochim. Acta* **2006,** *52* (3), 1329–1338.
(21) Katsounaros, I.; Dortsiou, M.; Polatides, C.; Preston, S.; Kypraios, T.; Kyriacou, G., Reaction pathways in the electrochemical reduction of nitrate on tin. *Electrochim. Acta* **2012,** *71*, 270–276.

(22) Akhade, S. A.; Bernstein, N. J.; Esopi, M. R.; Regula, M. J.; Janik, M. J., A simple method to approximate electrode potential-dependent activation energies using density functional theory. *Catal. Today* **2017,** *288*, 63–73.
(23) Luo, W.; Nie, X.; Janik, M. J.; Asthagiri, A., Facet dependence of CO_2 reduction paths on Cu electrodes. *ACS Catal.* **2016,** *6* (1), 219–229.
(24) Jitariu, L.; Hirst, D., Theoretical investigation of the potential energy surface for the reaction of NO_3 with H. *Phys. Chem. Chem. Phys.* **1999,** *1* (6), 983–987.
(25) Chen, G.-F.; Yuan, Y.; Jiang, H.; Ren, S.-Y.; Ding, L.-X.; Ma, L.; Wu, T.; Lu, J.; Wang, H., Electrochemical reduction of nitrate to ammonia via direct eight-electron transfer using a copper–molecular solid catalyst. *Nat. Energy* **2020,** *5* (8), 605–613.
(26) Wang, Y., Zhou, W., Jia, R., Yu, Y. & Zhang, B. Unveiling the activity origin of a copper-based electrocatalyst for selective nitrate reduction to ammonia. *Angew. Chem.* **2020,** 132, 5388–5392.
(27) Wang, Y. *et al.* Enhanced nitrate-to-ammonia activity on copper–nickel alloys via tuning of intermediate adsorption. *J. Am. Chem. Soc.* **2020,** 142, 5702–5708.
(28) Abdallah, R.; Geneste, F.; Labasque, T.; Djelal, H.; Fourcade, F.; Amrane, A.; Taha, S.; Floner, D., Selective and quantitative nitrate electroreduction to ammonium using a porous copper electrode in an electrochemical flow cell. *J. Electroanal. Chem.* **2014,** *727*, 148–153.
(29) Xianbiao Fu, X. Z., Xiaobing Hu, Kun He, Yanan Yu, Tao Li, Qing Tu, Xin Qian, Qin Yue, Michael R. Wasielewski, Yijin Kang. , Alternative route for electrochemical ammonia synthesis by reduction of nitrate on copper nanosheets. *Appl. Mater. Today* **2020,** *19*, 100620.
(30) Deng, X.; Yang, Y.; Wang, L.; Fu, X. Z.; Luo, J. L., Metallic Co Nanoarray Catalyzes Selective NH_3 Production from Electrochemical Nitrate Reduction at Current Densities Exceeding 2 A cm^{-2}. *Adv. Sci.* **2021**, 2004523.
(31) Yu, Y.; Wang, C.; Yu, Y.; Wang, Y.; Zhang, B., Promoting selective electroreduction of nitrates to ammonia over electron-deficient Co modulated by rectifying Schottky contacts. *Sci. China Chem.* **2020,** *63* (10), 1469–1476.
(32) Yin, H.; Peng, Y.; Xiong, S.; Chen, J.; Wang, C.; Wang, R.; Chen, Z.; Kuwahara, Y.; Luo, J.; Yamashita, H., Alloying effect-induced electron polarization drives nitrate reduction to ammonia. **2020**.
(33) McEnaney, J. M.; Blair, S. J.; Nielander, A. C.; Schwalbe, J. A.; Koshy, D. M.; Cargnello, M.; Jaramillo, T. F., Electrolyte Engineering for Efficient Electrochemical Nitrate Reduction to Ammonia on a Titanium Electrode. *ACS Sustain. Chem. Eng.* **2020,** *8* (7), 2672–2681.
(34) Jia, R.; Wang, Y.; Wang, C.; Ling, Y.; Yu, Y.; Zhang, B., Boosting Selective Nitrate Electroreduction to Ammonium by Constructing Oxygen Vacancies in TiO_2. *ACS Catal.* **2020**, 3533–3540.
(35) Zhu, J. Y.; Xue, Q.; Xue, Y. Y.; Ding, Y.; Li, F. M.; Jin, P.; Chen, P.; Chen, Y., Iridium Nanotubes as Bifunctional Electrocatalysts for Oxygen Evolution and Nitrate Reduction Reactions. *ACS Appl. Mater. Interfaces* **2020,** *12* (12), 14064–14070.
(36) Li, J.; Zhan, G.; Yang, J.; Quan, F.; Mao, C.; Liu, Y.; Wang, B.; Lei, F.; Li, L.; Chan, A. W. M.; Xu, L.; Shi, Y.; Du, Y.; Hao, W.; Wong, P. K.; Wang, J.; Dou, S. X.; Zhang, L.; Yu, J. C., Efficient Ammonia Electrosynthesis from Nitrate on Strained Ruthenium Nanoclusters. *J. Am. Chem. Soc.* **2020,** *142* (15), 7036–7046.
(37) S. H&old, K.-D. V., T. Tacke and M. Sellb, Development of catalysts for a selective nitrate and nitrite removal from drinking water. *Catal. Today* **1993,** *17*, 21–30.
(38) Polatides, C.; Kyriacou, G., Electrochemical reduction of nitrate ion on various cathodes ? reaction kinetics on bronze cathode. *J. Appl. Electrochem.* **2005,** *35* (5), 421–427.
(39) Su, J. F.; Kuan, W.-F.; Liu, H.; Huang, C. P., Mode of electrochemical deposition on the structure and morphology of bimetallic electrodes and its effect on nitrate reduction toward nitrogen selectivity. *Appl. Catal. B* **2019,** *257*.
(40) Dortsiou, M.; Kyriacou, G., Electrochemical reduction of nitrate on bismuth cathodes. *J. Electroanal. Chem.* **2009,** *630* (1-2), 69–74.

(41) Teng, W.; Bai, N.; Liu, Y.; Liu, Y.; Fan, J.; Zhang, W. X., Selective Nitrate Reduction to Dinitrogen by Electrocatalysis on Nanoscale Iron Encapsulated in Mesoporous Carbon. *Environ. Sci. Technol.* **2018,** *52* (1), 230–236.
(42) Kuang, P.; Natsui, K.; Feng, C.; Einaga, Y., Electrochemical reduction of nitrate on boron-doped diamond electrodes: Effects of surface termination and boron-doping level. *Chemosphere* **2020,** *251*.
(43) Hossain, M. M.; Kawaguchi, T.; Shimazu, K.; Nakata, K., Reduction of nitrate on tin-modified palladium-platinum electrodes. *J. Electroanal. Chem.* **2020,** *864*, 114041.
(44) Shih, Y.-J.; Wu, Z.-L.; Lin, C.-Y.; Huang, Y.-H.; Huang, C.-P., Manipulating the crystalline morphology and facet orientation of copper and copper-palladium nanocatalysts supported on stainless steel mesh with the aid of cationic surfactant to improve the electrochemical reduction of nitrate and N_2 selectivity. *Appl. Catal. B.* **2020,** *273*, 119053.
(45) Sanjuán, I.; García-Cruz, L.; Solla-Gullón, J.; Expósito, E.; Montiel, V., Bi–Sn nanoparticles for electrochemical denitrification: activity and selectivity towards N_2 formation. *Electrochim. Acta* **2020,** *340*, 135914.
(46) Beltrame, T. F.; Gomes, M. C.; Marder, L.; Marchesini, F. A.; Ulla, M. A.; Bernardes, A. M., Use of copper plate electrode and Pd catalyst to the nitrate reduction in an electrochemical dual-chamber cell. *J. Water Process. Eng.* **2020,** *35*, 101189.
(47) Shih, Y.-J.; Wu, Z.-L.; Huang, Y.-H.; Huang, C.-P., Electrochemical nitrate reduction as affected by the crystal morphology and facet of copper nanoparticles supported on nickel foam electrodes (Cu/Ni). *Chem. Eng. J.* **2020,** *383*, 123157.
(48) Su, J. F.; Kuan, W.-F.; Chen, C.-L.; Huang, C.-P., Enhancing electrochemical nitrate reduction toward dinitrogen selectivity on Sn-Pd bimetallic electrodes by surface structure design. *Appl. Catal. A-Gen.* **2020,** *606*, 117809.
(49) Shih, Y.-J.; Wu, Z.-L., Electroplating of surfactant-modified tin catalyst over a nickel foam electrode (Sn/Ni) for selective N_2 yield from nitrate reduction as affected by Sn (200) and Sn (101) crystal facets. *Appl. Catal. B.* **2021,** *285*, 119784.
(50) Liu, Z.; Dong, S.; Zou, D.; Ding, J.; Yu, A.; Zhang, J.; Shan, C.; Gao, G.; Pan, B., Electrochemically mediated nitrate reduction on nanoconfined zerovalent iron: Properties and mechanism. *Water Res.* **2020,** *173*, 115596.
(51) Guo, S.; Heck, K.; Kasiraju, S.; Qian, H.; Zhao, Z.; Grabow, L. C.; Miller, J. T.; Wong, M. S., Insights into Nitrate Reduction over Indium-Decorated Palladium Nanoparticle Catalysts. *ACS Catal.* **2017,** *8* (1), 503–515.
(52) Marchesini, F. A.; Picard, N.; Miró, E. E., Study of the interactions of Pd,In with SiO2 and Al2O3 mixed supports as catalysts for the hydrogenation of nitrates in water. *Catal. Commun.* **2012,** *21*, 9–13.
(53) Constantinou, C. L.; Costa, C. N.; Efstathiou, A. M., Catalytic removal of nitrates from waters. *Catal. Today* **2010,** *151* (1-2), 190–194.
(54) Hamid, S.; Kumar, M. A.; Lee, W., Highly reactive and selective Sn-Pd bimetallic catalyst supported by nanocrystalline ZSM-5 for aqueous nitrate reduction. *Appl. Catal. B* **2016,** *187*, 37–46.
(55) Kobune, M.; Takizawa, D.; Nojima, J.; Otomo, R.; Kamiya, Y., Catalytic reduction of nitrate in water over alumina-supported nickel catalyst toward purification of polluted groundwater. *Catal. Today* **2020,** *352*, 204–211.
(56) Bradu, C.; Căpăţ, C.; Papa, F.; Frunza, L.; Olaru, E.-A.; Crini, G.; Morin-Crini, N.; Euvrard, E.; Balint, I.; Zgura, I., Pd-Cu catalysts supported on anion exchange resin for the simultaneous catalytic reduction of nitrate ions and reductive dehalogenation of organochlorinated pollutants from water. *Appl. Catal. A-Gen.* **2019,** *570*, 120–129.
(57) Santos, A.; Restivo, J.; Orge, C. A.; Pereira, M. F. R.; Soares, O., Nitrate Catalytic Reduction over Bimetallic Catalysts: Catalyst Optimization. *C* **2020,** *6* (4), 78.
(58) Smith, J. C.; Clark, C., The Future's Energy Mix: The Journey to Integration [Guest Editorial]. *IEEE Power and Energy Magazine* **2019,** *17* (6), 19–23.
(59) Miller, E. L. In *Hydrogen Production & Delivery Program-Plenary Presentation*, US DOE Annual Merit Review and Peer Evaluation Meeting, **2017**.

(60) Hunt, A. J.; Sin, E. H.; Marriott, R.; Clark, J. H., Generation, capture, and utilization of industrial carbon dioxide. *ChemSusChem: Chemistry & Sustainability Energy & Materials* **2010,** *3* (3), 306–322.
(61) Seidel, C.; Gorman, C.; Darby, J.; Jensen, V., An assessment of the state of nitrate treatment alternatives. *Final Report of the American Water Works Association, Inorganic Contaminant Research & Inorganic Water Quality Joint Project Committees* **2011**, 118–121.

Author Contributions

W.L., L.T.R., and B.H.S. conceived and supervised the project. H.L. and Y.Q. performed the electrochemical measurements. H.L. and Y.Chen carried out the physical characterization. J.P. and K.S. carried out the DFT calculations. H.L., Y.Chen, and Y.Cheng performed the studies on the catalytic reduction of nitrite. S.G. helped with the design of the reactors for the electrocatalytic and catalytic activity measurements. All authors discussed the results and contributed to the manuscript writing.